SESAR Engage KTN – PhD final report

PhD title:	Advanced Statistical Signal Processing for Next Generation Trajectory Prediction
Candidate's name:	Homeyra Khaledian
Lead supervisor's name:	Xavier Prats
Co-supervisor's name (if applicable):	Jordi Vilà-Valls
Proponent institute:	Universitat Politècnica de Catalunya (UPC)
Consortium institutes (if applicable):	-
Thematic challenge:	TC2 Data-driven trajectory prediction
Edition date:	05 July 2022
Edition:	1.1
Dissemination level:	Public

This project has received funding from the SESAR Joint Undertaking under the European Union's Horizon 2020 research and innovation programme under grant agreement No 783287.

1. Abstract

Accurate and reliable trajectory prediction (TP) is required in several air traffic management (ATM) systems, for instance, to design air and ground-based decision support tools and safety nets. Estimating the aircraft trajectory in the vertical plane typically requires the knowledge of a pair of aircraft intents (e.g., constant Mach and minimum throttle), information which is seldom available, besides for the ownship (i.e., one's own aircraft) trajectory planning system. In the flight execution phase, the aircraft is directed by the (auto) pilot through a series of sequential guidance modes that might override some of the planning phase aircraft intents. Thus, guidance mode is defined as a combination of constraints/commands that specify how the aircraft should behave to perform a desired trajectory.

Reliable guidance mode information is fundamental for next generation of air- or ground-based TP, especially in the context of trajectory-based operations (TBO) and advanced decision support tools for aircraft crew and/or air traffic control e.g., to improve conflict detection (and resolution) algorithms, conformance monitoring, departure/arrival managers, separation assurance systems, etc. These new tools might result in increased safety, capacity, predictability and cost-efficiency for the future European ATM system.

This research is concentrated on identifying aircraft guidance modes in the vertical plane. The final goal of this study is to indicate that acquiring the knowledge of aircraft guidance mode significantly affects the TP problem, and subsequently, the new ATM systems. In this PhD i) we provided a new probabilistic perspective of the trajectory prediction problem using signal processing mathematical tools, ii) we review state-of-the-art and the main challenges for the design of novel or enhanced TP systems that should enable future ATM paradigms, iii) we develop an optimal guidance mode identification using a Kalman filtering approach, iv) we analyse the impact of model mismatch on the interacting multiple model (IMM) filtering technique, v) we propose a robust linear-constrained IMM filtering under model mismatch, vi) we also propose a new methodology based on Bayesian inference to identify the aircraft guidance modes, and finally, vii) we evaluate the methodology to indicate the effect of known guidance modes on the TP accuracy.

2. Objective of the study

Towards identifying the guidance mode and improve the trajectory prediction (TP) problem, the following main objectives have been achieved:

1. Review the state-of-the-art in guidance mode identification, TP problem, filtering technique, and main challenges in the new generation of ATM systems.
2. Probabilistic characterisation of guidance mode identification, and formal analysis on the limitations of standard filtering techniques (i.e., impact of a misspecified system);
3. Optimal guidance mode identification for centralised ground-based TP;
4. Robustification of the current filtering techniques and development of new robust approaches for TP (i.e., relying on linearly constrained filtering);
5. Bayesian sigma-point filtering technique to cope with nonlinear dynamics.

In this study, the knowledge of aircraft performance models is taken into account to build a solid system model for the TP purpose. Although the solution proposed in this PhD is a physical model-

based method, it is completely aligned with the objective of the second Engage thematic challenge (TC2) titled “data-driven trajectory prediction”. Identification of aircraft guidance mode in the flight execution phase is an achievement affecting TP. Outcome of this research fulfils the Engage TC2 expectations, including improvements in TP.

3. Motivation

Solving an important missing point in avionics or ground-based systems (i.e., identifying aircraft guidance modes) motivated us to define this PhD topic. Moreover, signal processing techniques and stochastic approaches have been applied to address tracking problems for several decades. In the problem at hand, using stochastic signal processing tools builds the framework of proposed methodology to address an interdisciplinary problem. This work started with the aim of enhancing the accuracy and precision of TP to cope with challenges in the new generation of the ATM systems. Therefore, enhancing the ground-based TP accuracy can positively affect the new ATM systems, for instance, improving conflict detection and resolution (CDR) methods and creating the foundation for self-separation applications, for instance.

4. Advances this work has provided with regard to the state of the art

Several approaches focusing on TP are available in the literature, which can be mainly divided in two groups: machine learning (ML) techniques and stochastic methods. A brief review of some real-time TP methods is provided hereafter.

In line with the current trend of using ML to solve any engineering problem, TP is not an exception. A comprehensive survey on ML-based TP is given in [26]. A possible approach to predict aircraft trajectories is to resort to neural networks (NNs), as proposed in [27].

The NN can be trained using a real trajectory database, allowing the system to perform strategic and/or tactical TP forecast in the planning and/or execution phases. For instance, an NN-based solution was proposed in [28] for terminal manoeuvring area applications to address the short-term 4D TP problem. The idea was to implement a combination of a sophisticated pre-processing stage, subsequently feeding a multi-cells NN to predict the trajectory. A different approach was presented in [24], where a Long-Short Term Memory solution was used for real-time estimation of some aircraft on-board parameters (i.e., fuel flow rate, landing gear and flap configuration settings). For this purpose, Flight Data Recorder data was used to train a model and ADS-B data was used to feed an NN structure.

ML-based approaches may be interesting if large data sets are available, but they also have several limitations: i) lack of understanding of the system behaviour; ii) it is not possible to theoretically assess performance limits; iii) the knowledge of physical parametric models is disregarded; and iv) for safety-critical applications it is unlikely that they could be certified.

A completely different TP approach is to rely on stochastic methods, which rather than learning the system as a black box, exploit the physical knowledge of the TP problem at hand, and therefore have been widely studied in the literature. Such physical modelling can be expressed for instance in state-space form, including: i) the dynamic aircraft model (e.g., the point-mass model); ii) the available data (e.g., ADS-B data, EHS data, and extended projected profile (EPP) [16,17]); and iii) the system uncertainty, which has been studied in detail for instance in [29,30]. In this case, TP is an estimation problem, and one can resort to the vast literature on estimation methods. Some relevant contributions are provided in the sequel.

An adaptive algorithm was proposed in [31] to improve the TP accuracy for short look-ahead times in the climbing phase. Such adaptive algorithm dynamically adjusts the modelled aircraft weight based

on observed radar track data. In [32], a stochastic linear hybrid system was introduced to model the aircraft motion with changing flight modes for 4D TP and conflict detection problems. Such a probabilistic approach combined the aircraft dynamics with flight intent information to provide more reliable prediction results. Results showed that this intent-based TP approach was more accurate than other non-intent-based TP methods.

Kalman filter based methods provide the optimal recursive estimation solution if a single linear state-space model applies, and multiple model (MM) techniques such as the IMM filter must be considered when several dynamic system models appear [33] (e.g., guidance modes). In [34] a MM filter, based on 2-dimensional (2D) kinematic models, was used to improve aircraft tracking for CDR applications. Similarly, in [35] a MM filter was developed to identify aircraft manoeuvres during taxi operations. An enhanced MM filter, using a non-linear point mas model to describe 3-dimensional (3D) aircraft dynamics, was proposed in [36], showing significant benefits in terms of position estimation accuracy and filter robustness with respect to conventional kinematic-based filters. But all these works aimed at identifying simple manoeuvres in the horizontal plane, such as coordinated turns, constant speed or acceleration segments, then not being suited for the TP problem at hand.

In [37, 38] manoeuvres in the vertical plane were considered, but the algorithm was limited to identify simple manoeuvres such as constant altitude rate at constant speed. These limitations were partially addressed in [1], where a set of modes for a typical aircraft descent phase were taken into account to improve TP capabilities in the flight execution phase, being the starting point of this PhD. The real-time guidance mode identification problem was presented in a conference paper [1], where a sequence of guidance modes was identified using IMM filtering techniques in a vertical plane at altitude above 3000 [ft]. The purpose of the research was improving the accuracy of short-term aircraft TP in a typical aircraft descent. This PhD complements and extends the work done in [1]. Although the research done in [1] is remarkable, many missing challenges in the guidance mode identification problem need to be addressed. The outcome of this PhD provides some advances compared with the main reference (i.e., [1]), including: i) a statistical analysis is performed to assess the proposed method; ii) more validation trajectories containing real trajectories are considered; iii) the most complex parts of an aircraft trajectory—between FL100 and 50 ft above the runway—are analysed; iv) aircraft high-lift devices and landing gear deployment are modelled; v) the first moment of flap deployment/retraction is estimated; and vi) mathematical details and explanations are added. All the advances are placed in chapter 3 (i.e., optimal real-time guidance mode identification in a vertical plane) of dissertation.

5. Methodology

Filtering techniques are applied to identify a sequence of aircraft guidance modes. In this PhD, methods based on Kalman and particle filtering are taken into account to tackle the tracking problem. As stated in the literature review, Kalman-based filters are quite a powerful tool for the TP problem although these methods require a perfect knowledge of the system. For instance, process and measurement functions, the corresponding noise statistics, and input parameters are required to be known in a Kalman-based filter method, either for linear or non-linear systems. In practice, the perfect knowledge of the system may not be accessible. Therefore, towards improving the TP accuracy and precision in real-life applications, particle filtering is a well-performed method to tackle the unknown initialization and uncertainties (with non-Gaussian noise distribution). Particle filtering as a specific sequential Monte Carlo simulation method, is a recursive Bayesian estimator based on importance sampling. In the particle filtering method, the state vector is estimated recursively from the measurements.

Generally speaking, filtering distribution is defined as $p(x_t|y_{0:t})$, and tracking in filtering is obtaining $p(x_t|y_{0:t})$ from $p(x_{t-1}|y_{0:t-1})$. In case of independent noise samples, using the Bayes theorem and joint probability distribution, the recursive equation to obtain $p(x_{0:t}|y_{0:t})$ from $p(x_{0:t-1}|y_{0:t-1})$ is given by:

$$p(x_{0:t}|y_{0:t}) = \frac{p(y_t|x_t)\,p(x_t)}{p(y_t)}\,p(x_{0:t-1}|y_{0:t-1})\,;\; p(x_t) = p(x_t|x_{t-1})\;\&\;p(y_t) = p(y_t|y_{0:t-1})\;\;.$$

In real-life applications, obtaining $p(x_t|y_{0:t})$ from $p(x_{t-1}|y_{0:t-1})$ is based on approximations. In filtering methods, the extended Kalman filter (EKF) linearizes the system model around the estimated state vector and its corresponding covariance, while the particle filtering approximates the distribution for tracking. It is worth mentioning that the measurements are not observed continuously. Therefore, the approximation for the distribution is given by discrete random measures defined by particles and their corresponding weights. Tacking into account I random measures, $x^{(i)}; i = 1{:}I$ as particles with their weights, $w^{(i)}; i = 1{:}I$, the approximation of the distribution is computed as $p(x) \simeq \sum w^{(i)}\delta(x - x^{(i)})$, where $\delta(.)$ is the Dirac delta function [12]. Therefore, the main difference between EKF and particle filtering is the approximation of the distribution. In the following, the optimal Kalman-based filtering method is explained for the application at hand.

In practice, the lateral path uncertainty is low [2], while the vertical profile is more uncertain and complex. Therefore, the focus of this research is on the vertical profile. At each moment, the aircraft is steered with one guidance mode (i.e., a pair of constraints/commands).

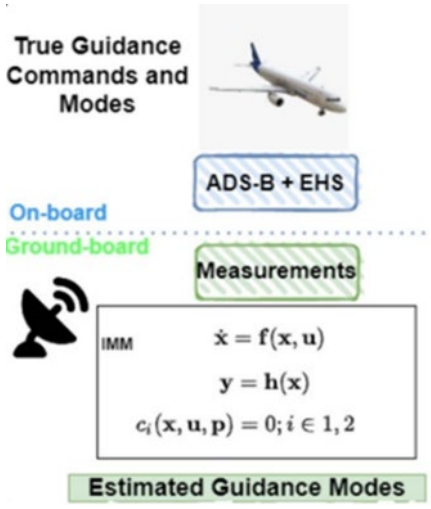

Fig. 1: General workflow.

IMM approach is used for ground-based identification of guidance mode among all possible guidance modes in the vertical profile. In addition to the mode identification, the aircraft trajectory estimation is obtained from the IMM method by observing surveillance data. Figure [1] shows the general system workflow under consideration. As depicted in Figure [1], on-board the aircraft is steered with guidance commands and Automatic Dependent Surveillance-Broadcast (ADS-B) and Enhanced Mode-S Surveillance (EHS) data are received to the ground. In this figure, x , y and u are the state, measurement, and control vector, respectively. The movement of the aircraft is modelled in its vertical plane to form the system model based on three main equations: i) $\dot{x} = f(x, u)$ describes the process model or state evaluation. ii) $y = h(x)$ provides the link between the measurements and the state to be inferred. iii) In order to derive the motion equations, each guidance command pair is associated to a pair of algebraic expressions (i.e., c_1 and c_2) that relate the guidance commands of each mode and the control vector (denoted $u(p, x)$ to emphasise this dependency). More details on aircraft trajectory planning and execution, guidance modes, filtering techniques, and system model are described in the sequel.

5.1 Aircraft Trajectory Planning and Execution

Modern aircraft have high levels of flight automation, mostly implemented in what is commonly named as the FMS. Some aircraft models use slightly different names, such as certain Airbus models with the flight management and guidance system (FMGS) or even the flight management, guidance and envelope computer (FMGEC), in order to emphasise additional functionalities of those systems. In this study, however, we use the rather generic name of FMS to refer to the systems on-board

providing flight trajectory planning and guidance. Among other functionalities, the FMS is in charge to first plan a trajectory; and then, support the (automatic) execution of the trajectory, providing guidance commands to the autopilot or to the flight director if the aircraft is manually flown.

Before take-off, the FMS generates the most cost-efficient trajectory plan. The planned trajectory complies with all operational and flight envelope constraints, including potential ATM constraints depicted in the departure procedure. Similarly, the FMS generates a new trajectory plan in cruise, before starting the descent; or at any point if manually triggered by the pilot.

Planned trajectories are just that: a plan. Then, they have to be materialised or executed in flight. For this purpose, the FMS has a variety of guidance modes and functionalities in order to follow the trajectory plan and to react in different ways in case that deviations from the plan occur.

This section describes the mathematical process that underpins the computation (planning) and execution (guidance) of realistic aircraft trajectories.

Mathematically speaking, the motion of an aircraft can be described by a system of ordinary differential equations (ODEs), derived from the combination of translational (force) and rotational (moment) equations of movement. Although this six degrees of freedom model results in the most accurate planning of an aircraft trajectory, it requires an extensive aerodynamic and propulsive model and the knowledge of the inertia tensor of the aircraft. For trajectory planning purposes in the FMS, the aircraft rotational rate is small and fast enough to consider only the translational equations of movement, leading to a three degrees of freedom (3DoF) model [3]. In fact, some ATM applications use even simpler models, such as total energy models or pure kinematic models [4].

The 3DoF model considers the aircraft as a point mass. In this model, the centre of mass is considered as the rotational centre where all forces apply. A further simplification of the 3DoF point-mass model in a vertical plane results in the so-called gamma-command model [5]. The vertical equilibrium is assumed in the gamma-command model. This is the model considered in this PhD:

$$\frac{dh}{dt} = vsin(\gamma) \tag{1.1}$$

$$\frac{ds}{dt} = \sqrt{v^2 cos^2(\gamma) - W_x^2} + W_s \tag{1.2}$$

$$\frac{dv}{dt} = \frac{T(,v,h) - D(v,h,m,\chi)}{m} - gsin(\gamma) \tag{1.3}$$

$$\frac{dm}{dt} = -q(T,v,h) \tag{1.4}$$

where the state vector, $x = [h, s, v, m]^T$, is composed of the geometric altitude, the along path distance, the true airspeed, and the mass of the aircraft; and the generic control vector of this model, $u = [\gamma, \pi]^T$, is given by the aerodynamic flight path angle (FPA) and the engine throttle. T is the total thrust delivered by the aircraft engines, D is the aerodynamic drag, q is the total fuel flow, W_x is the cross-wind component, W_s is the along path wind component, and g is the gravitational acceleration. It is worth noting that D also depends on the setting of the high-lift devices (i.e. flaps and/or slats) and landing gear. This aircraft configuration is denoted in the equations above by χ.

The total engine thrust is given by the following expression:

$$T = T_{idle} + \pi(T_{max} - T_{idle}) \tag{2}$$

Where T_{idle} is the residual thrust delivered by the engines in idle setting ($\pi = 0$) and T_{max} is the thrust delivered for the maximum throttle setting ($\pi = 1$).

An aircraft performance model is required to model D, T_{idle}, T_{max}, and q, as a function of (some of) the state variables; while a weather model is also required to model the wind components appearing in Equations (1.1-1.4), but also to model certain aircraft performance variables that typically depend on air temperature and/or pressure.

Note that two degrees of freedom must be closed in order to integrate Equations (1.1-1.4) along time. However, they are seldom given in terms of throttle (π) and/or flight path angle (γ) functions of the time. Instead, the aircraft trajectory is typically divided in different phases or segments, and most of them are operated at constant Mach or constant calibrated airspeed, for instance. In some cases climbs/descents could be specified at a constant vertical speed (i.e. rate of climb/descent) and acceleration/deceleration segments are computed keeping a constant energy share factor (i.e., a parameter that specifies the ratio of the available thrust that is allocated to gain/lose kinetic energy as opposed to gain/lose potential energy). Thus, in a more generic formulation, two path constraints (c_1 and c_2), also known as aircraft intents [6], shall be taken into account to mathematically close Equations (1.1-1.4), rather than just assuming a given control vector u:

$$c_i(x, u, p) = 0\ ;\ i \in \{1,2\} \tag{3}$$

where p is a vector of known parameters. For each path constraint a parameter among a set of known parameters is fixed in order to form the p vector. For instance, the calibrated airspeed value in a constant speed segment, the throttle setting in a constant throttle segment, etc.

Equations (1.1-1.4) and (3) together form a system of differential-algebraic equations (DAEs) that fully describe a trajectory in the vertical plane. Unless π and γ are directly given as a known input control sequence, it will be always needed to compute them first, in order to transform the original set of DAEs to a system of ODEs suitable for numerical integration.

5.2 Aircraft Trajectory Guidance

This section focuses on the guidance strategies that are relevant for this work, which are the estimation targets of the IMM-based methods.

Assuming the FMS had perfect models when planning the trajectory, this would lead to the same 4D trajectory (and fuel consumption) as theoretically planned. Nevertheless, in a real flight, different sources of uncertainty would be present, such as aircraft performance models, weather forecasts, actuator dynamics, etc. This means that the other variables that are not followed by the guidance system will differ from the plan. In the previous example, where the path and throttle plan were commanded (and therefore followed by the actuators), the aircraft would not follow the planned speed schedule due to uncertainties, and the final fuel consumption would also differ from the computed one at the planning stage. In case, for instance, that throttle plan and speed schedule are commanded, the actual path would differ from the planned one in presence of uncertainty.

The guidance function of the FMS contains, in fact, a quite complex logic of different guidance modes and strategies that are switched from one to another during the execution of the flight, depending on many input variables, such as the deviations with respect to the plan, the phase of the flight, operational conditions and flight envelope, capabilities of the actuators, etc.

The guidance commands considered in this work are listed, depicting at the same time, the (known) input guidance target associated to each of them:

1. MACH: Constant Mach number ($\bar{M}$)
2. CAS: Constant calibrated airspeed ($\bar{\tilde{v}}_{CAS}$)

3. DEC: Deceleration at a constant energy share factor ($\underline{k}$)
4. ACC: Acceleration at a constant energy share factor ($\underline{k}$)
5. THR: Fixed throttle setting ($\bar{\bar{\pi}}$)
6. VS: Constant vertical speed ($\bar{\bar{v}}_h$)
7. FPA: Constant ground flight path angle ($\bar{\bar{\gamma}}_g$)
8. ALT: Constant pressure altitude (zero vertical speed)
9. SPD: Constant speed ($\bar{M}$, $\bar{\bar{v}}_{CAS}$). Only used when the other guidance mode is ALT.

Table I lists all pairs of guidance commands considered in this paper. The first and second columns identify the guidance commands that direct, respectively, the two independent actuators of the aircraft (elevator and throttle). For each pair of commands, the parameters vector p (i.e., known input guidance target) is given in the third column of the table.

Table I: All possible guidance modes in the vertical profile considered in this PhD.

Command1	Command2	Parameters	Control vector
MACH		$p = [\bar{M}, \bar{\bar{\pi}}]$	eq.(4.1) and eq.(4.3)
CAS	THR	$p = [\bar{\bar{v}}_{CAS}, \bar{\bar{\pi}}]$	eq.(4.1) and eq.(4.4)
ACC/DEC		$p = [\underline{k}, \bar{\bar{\pi}}]$	eq.(4.1) and eq.(4.2)
	MACH	$p = [\bar{\bar{v}}_h, \bar{M}]$	eq.(4.7) and eq.(4.5)
VS	CAS	$p = [\bar{\bar{v}}_h, \bar{\bar{v}}_{CAS}]$	eq.(4.8) and eq.(4.5)
	ACC/DEC	$p = [\bar{\bar{v}}_h, \underline{k}]$	eq.(4.6) and eq.(4.5)
	MACH	$p = [\bar{\bar{\gamma}}_g, \bar{M}]$	eq.(4.7) and eq.(4.9)
FPA	CAS	$p = [\bar{\bar{\gamma}}_g, \bar{\bar{v}}_{CAS}]$	eq.(4.8) and eq.(4.9)
	ACC/DEC	$p = [\bar{\bar{\gamma}}_g, k]$	eq.(4.6) and eq.(4.9)
VS		$p = [\bar{\bar{v}}_h, \bar{\bar{\pi}}]$	eq.(4.1) and eq.(4.5)
FPA	THR	$p = [\bar{\bar{\gamma}}_g, \bar{\bar{\pi}}]$	eq.(4.1) and eq.(4.9)
ALT		$p = [\bar{\bar{v}}_h = 0, \bar{\bar{\pi}}]$	eq.(4.1) and eq.(4.10)
ALT	SPD	$p = [\bar{\bar{v}}_h = 0, \bar{M}]$	eq.(4.11) and eq.(4.10)

$$\pi(x,p) = \bar{\bar{\pi}} \tag{4.1}$$

$$\gamma(x,p) = arcsin\left(\frac{T_{idle}+\pi(T_{max}-T_{idle})-D}{mg}\underline{k}\right) \tag{4.2}$$

$$\gamma(x,p) = arcsin\left(\frac{T_{idle}+\pi(T_{max}-T_{idle})-D}{mg}\frac{1}{1-\frac{\lambda_\tau R\gamma_a}{2g}\bar{M}^2}\right) \tag{4.3}$$

$$\gamma(x,p) = arcsi\left(\frac{T_{idle}+\pi(T_{max}-T_{idle})-D}{mg}\frac{1}{1+\frac{A}{\delta}\left(\frac{A}{\delta}+1\right)^{\mu-1}-R\frac{\lambda_\tau}{\mu g}\left[\left(\frac{A}{\delta}+1\right)^{\mu}-1\right]}\right); \quad (4.4)$$

$$A = (1+\bar{\bar{v}}_{CAS}{}^2\frac{\mu\rho_0}{2p_0})^{\frac{1}{\mu}}-1$$

$$\gamma(x,p) = arcsin\left(\frac{\bar{\bar{v}}_h}{v}\right) \quad (4.5)$$

$$\pi(x,p) = \frac{D+\frac{1}{k}mgsin(\gamma)-T_{idle}}{T_{max}-T_{idle}} \quad (4.6)$$

$$\pi(x,p) = \frac{D+(1-\frac{\lambda_\tau R\gamma a}{2g}\bar{M}^2)mgsin(\gamma)-T_{idle}}{T_{max}-T_{idle}} \quad (4.7)$$

$$\pi(x,p) = \frac{D+(1+\frac{A}{\delta}\left(\frac{A}{\delta}+1\right)^{\mu-1}-R\frac{\lambda_\tau}{\mu g}\left[\left(\frac{A}{\delta}+1\right)^{\mu}-1\right])mgsin(\gamma)-T_{idle}}{T_{max}-T_{idle}} \quad (4.8)$$

$$\gamma(x,p) = arcsin\left(sin\left(\bar{\bar{\gamma}}_g\right)\left[\left(1-\bar{W}_x{}^2-\bar{W}_s{}^2sin^2\left(\bar{\bar{\gamma}}_g\right)\right)^{\frac{1}{2}}+\bar{W}_s cos\left(\bar{\bar{\gamma}}_g\right)\right]\right) \quad (4.9)$$

$$\gamma(x,p) = 0 \quad (4.10)$$

$$\pi(x,p) = \frac{D-T_{idle}}{T_{max}-T_{idle}} \quad (4.11)$$

The command pairs of Table I are grouped by families, separated by horizontal lines in the table. The first set of command pairs identified, direct a fixed throttle setting (π), while the elevator is used to command a certain speed or a certain acceleration/deceleration. These pairs of guidance commands are those typically found in climbs or descents. Aircraft typically climb at a fixed throttle setting (which could be the maximum climb engine rating, a take-off/go-around rating, a reduced thrust rating, etc.); while keeping a constant CAS in the lower parts of the climb, or a constant Mach in the higher parts of the climb phase. It is worth noting that in the lower atmosphere the maximum CAS in operations (named VMO) is more limiting than the maximum Mach in operations (MMO) and CAS is the operational speed used. At higher altitudes, however, MMO becomes more limiting than VMO and Mach number becomes the operational speed. Moreover, in a typical climb, different (short) acceleration phases are also found, and these are typically performed at a constant energy share factor (thus, accelerating and climbing at the same time). This energy share factor specifies the ratio of potential energy to the total energy (i.e., potential and kinetic energy). In other words, the aircraft flies at a constant ratio of rate of climb to acceleration. Symmetrically, a descent is typically performed at a constant throttle setting (at or close to idle thrust), with constant Mach descents at higher altitudes, followed by constant CAS descents at lower altitudes. Deceleration phases in descent are also performed at a given energy share factor, in general.

In the second set of command pairs, the elevator is commanded to keep a fixed vertical speed ($\bar{\bar{v}}_h$), while the throttle is then commanded to maintain a certain speed or a certain acceleration/deceleration. In a typical climb or descent, the (auto) pilot hardly ever steers the aircraft by keeping a constant rate of climb or descent. There are, however, some situations where these modes are used. For instance, in an early descent situation (when the air traffic controller clears the descent before reaching the top of descent planned by the FMS), the guidance system will typically command VS-MACH (which can be followed by a VS-CAS at lower altitudes) in order to intercept the planned descent from below [7]. This type of guidance might also be found in the so-called "re-pressurisation segments'', sometimes found at the beginning of the descent phase in which the vertical speed is limited to permit a proper cabin re-pressurisation. Furthermore, in certain situations the air traffic control might request the aircraft crew to climb/descend at a given (or minimum) rate

of climb/descent. In such situations, these guidance modes would also be triggered. The pairs VS-DEC and VS-ACC are seldom used in typical operations, but considered in our models for the sake of completeness.

The third set of pairs command the elevator to keep a fixed ground flight path angle ($\bar{\bar{\gamma}}_g$), while the throttle is commanded to maintain a certain speed or a certain acceleration/deceleration. Like the previous guidance family, these pairs are activated in very specific situations, especially in the descent phase. When an idle descent cannot be planned because of altitude and/or speed restrictions in the destination terminal airspace, the FMS typically plans segments of constant ground flight path angle that "geometrically" join certain navigation waypoints overflying them at specific altitudes. In those cases, FPA-MACH or FPA-CAS will be commanded. Another typical example is when the aircraft is established in the instrumental landing system glide slope, in the final approach segment. There, the aircraft would command either FPA-DEC if decelerating or FPA-CAS if keeping a constant airspeed (typically in the last part of the final approach, with the aircraft fully configured and stabilised for landing). The pair FPA-ACC is seldom used, but also kept here for completeness.

In the fourth set of command pairs, the elevator is dedicated to follow a specific vertical trajectory profile (either at constant vertical speed, constant ground flight path angle, or a constant pressure altitude), while a fixed throttle setting is given (π). These pairs are rarely used, except for the command pair ALT-THR, which is found in level-offs to (quickly) accelerate or decelerate the aircraft (depending on the thrust setting commanded).

Finally, the last command pair identified in Table I corresponds to the particular case where constant altitude and speed shall be followed. Since the pressure altitude is constant, keeping a constant Mach is equivalent to following a constant CAS and vice-versa. This corresponds to cruise flight, but also to level-offs at constant speed, typically found in terminal airspace when sequencing and merging traffic and/or for certain segments in the depart or approach procedures.

As explained, throttle and flight path angle together---i.e., the control vector used in Equations (1.1)-(1.4)---are seldom chosen as aircraft intents to plan a trajectory. Similarly, they are not typically used as guidance commands to steer the aircraft in the execution phase of the flight. Thus, in order to properly model all the different system models that arise from each possible pair of guidance commands identified in Table I, it is required to express this control vector as a function of the (known) guidance parameters for each pair. Similarly, this computation is also needed by the in-house trajectory simulator developed to generate validation trajectories in order to compute controls from a set of predefined aircraft intents. The mathematical relationship between intents (or guidance modes) and controls is given in the last column of Table I.

It is worth noting that, although the case studies presented in this paper assume no winds and international standard atmosphere (ISA) conditions---to express how the atmospheric properties (e.g., pressure, temperature, and density of air) change as a function of altitude---, for the sake of generality, Table I provides the expressions of the control vector when horizontal wind components and temperature/pressure deviations from ISA values are modelled.

5.3 Filtering techniques

State estimation is a fundamental task in a plethora of applications, i.e., robotics, tracking, guidance and navigation systems, to name a few [8, 9, 10]. In the case of discrete state-space models (SSMs), i.e., where we have a dynamic stochastic representation of both state and measurements, filtering refers to the estimation of x_k (at discrete time k) based on measurements up to discrete time k, typically denoted as: $\hat{x}_{k|k} \triangleq \hat{x}_{k|k}(y_1, \dots, y_k) = \hat{x}_{k|k}(\underline{y}_k)$, with $\underline{y}_k^T = (y_1^T, \dots, y_k^T)$.

For linear SSMs the best linear minimum mean square error (MMSE) filter is given by the well-known Kalman filter (KF) [10]. For nonlinear SSMs, a popular approach is to use a first order approximation of the nonlinear process and measurement functions, leading to EKF. More involved solutions are the so-called sigma-point Gaussian filters under the Gaussian assumption [11] or particle filtering for general nonlinear/non-Gaussian systems [12].

The nonlinear discrete state-space model can be written as a jump Markov system.

$$x_k = f_{k-1}(x_{k-1}, u_{k-1}(p(\theta_k), x_{k-1}), \theta_k) + w_{k-1} \quad (5.1)$$

$$y_k = h_k(x_k) + v_k \quad (5.2)$$

where $\theta_k \in \{1,2, \dots, N\}$ is the mode state, that is , each value of the discrete random variable θ_k leads to a different SSM. Here $f_{k-1}(\cdot)$ and $h_k(\cdot)$ are known nonlinear system model functions; w_{k-1} and v_k are the process and measurement noise.

The measurements available from ADS-B and EHS considered in this article are $y = [h_p, v_g, v_h, v_{CAS}, M]^T$; with $h_p$the pressure altitude, v_g the ground speed, v_h the aircraft (operational) vertical speed (i.e., the pressure altitude change rate), v_{CAS} the calibrated airspeed (taken from the indicated airspeed broadcast by ADS-B), and M the Mach number.

With respect to (1.1)-(1.4), two additional variables are considered: i) τ is the temperature, and ii) p is the air pressure. Then, the complete state to be inferred is $x = [h, s, v, m, \tau, p]^T$, with,

$$\frac{d\tau}{dt} = \dot{\tau} = \tau_h(h)\dot{h}\,, \frac{dp}{dt} = \dot{p} = p_h(\tau, p)\dot{h} \quad (6)$$

Where τ_h and p_h are, respectively, the partial derivative of the temperature and pressure with respect to the altitude. The complete process function is then obtained from (1.1)-(1.4), expressing the dynamics of the aircraft, and (6). Notice that the control vector $u = [\gamma, \pi]^T$ is rewritten as $u_{k-1}(p(\theta_k), x_{k-1})$, where at each time instant k, for the corresponding mode θ_k, the values of γ and π are detailed in Table I.

In this contribution, we consider that both process and measurement noise are Gaussian distributed, being a valid assumption under nominal conditions (i.e., no impulsive or heavy-tailed behaviours in the aircraft dynamics that can be assumed to be smooth, and electronic thermal noise in the measurement devices), $w_k \sim N(0, Q_k)$ and $v_k \sim N(0, R_k)$.

The nonlinear Bayesian filtering for the system in (5.1)-(5.2) does not admit a closed-form solution, and suboptimal techniques must be accounted for the nonlinear systems of interest, the best performance is typically obtained by resorting to the IMM particle filter [13], but the price to be paid is a high computational complexity. If noise distributions are Gaussian one can resort to sigma-point filter-based IMM approaches [14,11], which use a bank of sigma-point filters, each one matched to a given SSM. It turns out that for the problem at hand, and because we seek the optimal performance under nominal conditions (i.e., small noise assumption), the sigma-point filter and EKF performance is equivalent, therefore in this contribution, and without loss of generality, we consider an EKF-IMM (i.e., IMM filter with a bank of N EKFs). Fig. 2 depicts the specific workflow of the EKF-IMM algorithm: i) interaction (or reinitialisation); ii) model-based filtering; and iii) combination (estimate fusion).

The IMM-based filtering approach uses a bank of N filters each one matched to a single SSM, then computes the posterior mode probabilities $\{\mu_k^i = P(\theta_k = i|y_{1:k})\}_{i=1}^N$, with $y_{1:k}^T = [y_1^T, \dots, y_k^T]$, and constructs the final estimate/covariance as a combination of individual EKF estimates $\hat{x}_{k|k}^i$, with

associated covariance $P^i_{k|k}$. Then, the question is how to recursively compute the mode conditional $\hat{x}^i_{k|k}$, $P^i_{k|k}$, and μ^i_k.

Interaction step: If one considers a transition probability matrix Π where its elements $r_{ji} = P(\theta_k = i|\theta_{k-1} = j)$ define the probability to jump from mode j to mode i, the i-th mixed filter input is

$$\hat{x}^{0i}_{k-1|k-1} = \sum_{j=1}^{N} \quad \mu^{ji}_{k-1|k-1}\hat{x}^j_{k-1|k-1} \tag{7.1}$$

$$P^{0i}_{k-1|k-1} = \sum_{j=1}^{N} \quad \mu^{ji}_{k-1|k-1}[P^j_{k-1|k-1} + (\hat{x}^j_{k-1|k-1} - \hat{x}^{0i}_{k-1|k-1})(\cdot)^T] \tag{7.2}$$

With mixing probabilities,

$$\mu^{ji}_{k-1|k-1} = \frac{r_{ji}\mu^i_{k-1}}{\sum_{l=1}^{N} \quad \pi_{li}\mu^l_{k-1}} \tag{8}$$

Filtering step: In this step, each EKF is matched to a GM. The i-th EKF prediction and update equations are,

$$\hat{x}^i_{k|k-1} = f_{k-1}(\hat{x}^{0i}_{k-1|k-1}, u_{k-1}\big(p(i), \hat{x}^{0i}_{k-1|k-1}\big), i) \tag{9}$$

$$P^i_{k|k-1} = F^i_{k-1}P^{0i}_{k-1|k-1}(F^i_{k-1})^T + Q_{k-1} \tag{10}$$

$$S^i_{k|k-1} = H^i_k P^i_{k|k-1}(H^i_k)^T + R_k \tag{11}$$

$$K^i_k = P^i_{k|k-1}(H^i_k)^T(S^i_{k|k-1})^{-1} \tag{12}$$

$$\hat{x}^i_{k|k} = \hat{x}^i_{k|k-1} + K^i_k(y_k - h_k(\hat{x}^i_{k|k-1})) \tag{13}$$

$$P^i_{k|k} = (I - K^i_k H^i_k)P^i_{k|k-1} \tag{14}$$

where F^i_{k-1} is the Jacobian of $f_{k-1}(\cdot,\cdot,i)$ evaluated at $\hat{x}^{0i}_{k-1|k-1}$, and H^i_k is the Jacobian of $h_k(\cdot)$ evaluated at $\hat{x}^i_{k|k-1}$. Notice that $y_k - h_k(\hat{x}^i_{k|k-1})$ is the so-called innovation vector, with associated covariance $S^i_{k|k-1}$. This innovation carries information about the fit between the observed data and the model used to compute the estimate (i.e., model likelihood).

Mode probability update: The only missing point is how to update the mode probability μ^i_k from μ^i_{k-1}, which for a Gaussian systems is

$$\mu^i_k = \frac{N(\hat{y}^i_{k|k-1}, S^i_{k|k-1})\sum_{j=1}^{N} \quad \pi_{ji}\mu^j_{k-1}}{\sum_{l=1}^{N} \quad N(\hat{y}^l_{k|k-1}, S^l_{k|k-1})\sum_{j=1}^{N} \quad \pi_{ji}\mu^l_{k-1}} \tag{15}$$

Fusion step: The final estimate/covariance as

$$\hat{x}_{k|k} = \sum_{i=1}^{N} \quad \mu^i_k\hat{x}^i_{k|k} \tag{16.1}$$

$$P_{k|k} = \sum_{i=1}^{N} \quad \mu^i_k[P^i_{k|k} + (\hat{x}^i_{k|k} - \hat{x}_{k|k})(\cdot)^T] \tag{16.2}$$

where $\hat{x}^i_{k|k}$ is the i-th EKF estimate, and $P^i_{k|k}$the corresponding estimation error covariance.

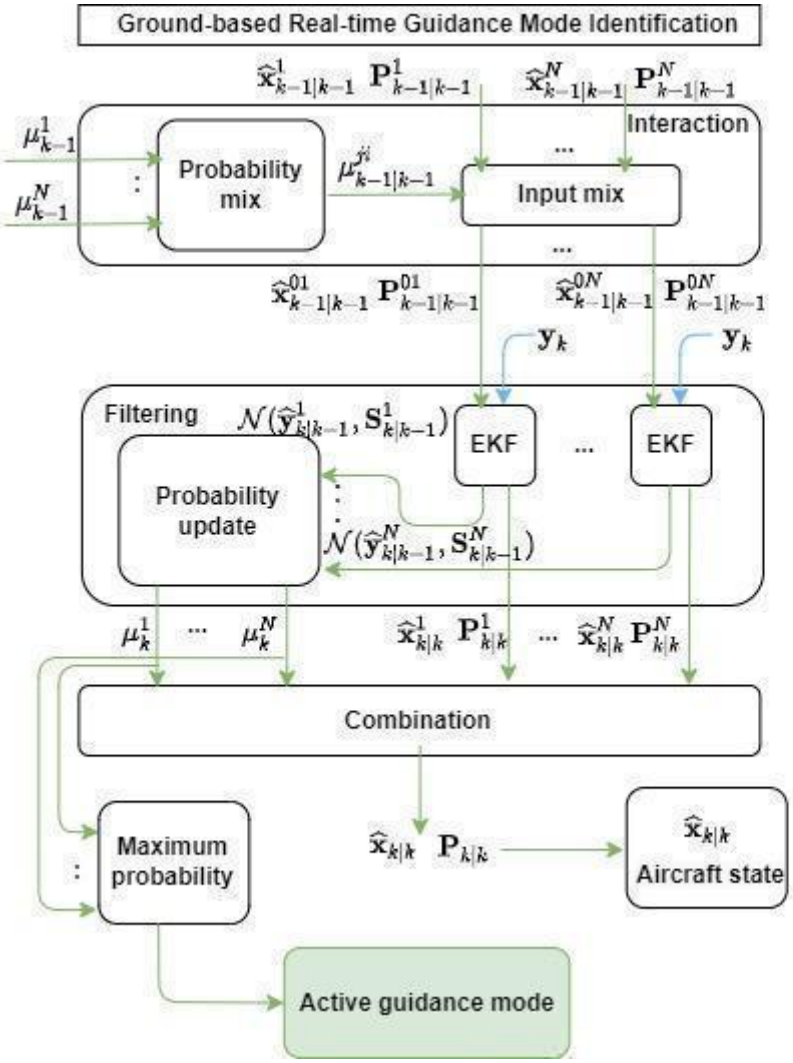

Fig. 2: The EKF-IMM flow diagram.

Guidance Mode Identification

Notice that the output of the EKF-IMM provides at each time step k the state vector estimate, $\hat{x}_{k|k}$, its associated covariance, $P_{k|k}$, but also the model probability for each guidance mode, μ_k^i. Even if it is not the standard use of IMM-based filters, μ_k^i can be exploited for model identification. Indeed, the estimated GM is taken as the one with largest mode probability (i.e., the most likely one),

$$\widehat{GM}_k = argmax\{[\mu_k^1, \dots, \mu_k^N]\}$$

Notice that the maximum mode probability will be larger if the different modes in the pool of candidates are very distinct, and lower if the modes are close to each other (i.e., competing modes). This implies that to obtain a good mode identification the user must avoid close or unidentifiable modes. Illustrative examples of this issue are shown in Section 8.2.

6. Description of the data the study relies on

In order to predict an accurate intruder trajectory (i.e., different from the ownship or corresponding aircraft's trajectory), the needed information of the aircraft (i.e., measurement vector) is typically obtained from surveillance systems. Traditionally, the aircraft azimuth is collected using the primary

surveillance radar (as a passive radar). In civil aviation, however, some additional information of the aircraft is transmitted by the aircraft transponder to the secondary surveillance radar (SSR) equipment: Mode-A transponders provide an aircraft identity by a 4-digit octal code; Mode-C transponders send as well the barometric altitude; and Mode-S transponders can be selectively interrogated to provide a more comprehensive set of aircraft information.

Moreover, the EHS technology is designed as a dependent protocol by secondary surveillance radar to improve all sorts of ATC systems by providing additional parameters. In fact, EHS provides the true airspeed, indicated airspeed, ground speed, Mach number, and true heading of the aircraft. Several Comm-B Data Selector (BDS) messages are identified as EHS: i) vertical intention report from BDS 40 (select altitude, barometric pressure setting); ii) track and turn report from BDS 50 (roll angle, track angle, ground speed, track angle rate, true airspeed); and iii) heading and speed report from BDS 60 (magnetic heading, indicated airspeed, Mach number, vertical velocity).

ADS-B is a newer data source using an automatically broadcasting technology and independent protocol. ADS-B is a data-link-based surveillance technology that can be exploited for both air-ground and air-air applications. This allows aircraft to send the identification, position, speed, and other flight parameters, which come from the on-board air data and navigation systems. Flight parameters such as rate of climb/descent, which is the time derivative of the pressure altitude; or inertial vertical speed, which is the time derivative of the geometric altitude [15].

Additionally, new automation and shared data within the TBO paradigm is raised to predict and share very accurate trajectory data via ADS - Contract Extended Projected Profile (ADS-C EPP) reports. Indeed, the EPP trajectory down-link standard is implemented to enable air-ground trajectory synchronisation [16,17] and likewise, to provide methods to extract some useful parameters such as rate of climb and descent, from EPP data [18]. General speaking, EPP provides some information (e.g., current and predicted gross weight, predicted speed profile, etc.) to enhance the performance and accuracy of ground-based TPs and ultimately, to improve ATC DSTs [18].

Moreover, in this research, a custom trajectory simulator is provided to generate desired trajectories and cope with the lack of real datasets. The custom trajectory simulator is used to generate 3D climb/descent trajectories (2D in the vertical plane plus time), which builds upon a gamma-command aircraft motion model [5], and the Eurocontrol's Base of Aircraft Data (BADA) v4.1 aircraft performance model [19]. The latter is used to define, for instance, the aircraft forces (e.g., thrust and drag) and fuel flow. A performance model of a representative narrow-body airliner has been chosen. The custom trajectory simulator emulates data based on real trajectories. Indeed, emulated profiles are inspired by comprehensive experimental analysis on real data and flight experiments.

The main challenge in the real scenario is having access to a flight data recorder (FDR)---the most accurate aircraft data to provide a “ground truth” for validation. Based on airline policies, data are not likely to be shared for research purposes. In addition to FDR, ADS-B and EHS data are obtainable through secondary surveillance radars. Some companies (e.g., OpenSky [20], flightradar24, and FlightAware) provide secondary surveillance radar data, mostly ADS-B, but with some limitations. For instance, secondary surveillance radars do not have a worldwide coverage, or only data after 2013 is available. OpenSky is free of cost, nevertheless, does not cover globally. Among other websites, flightradar24 [21] is able to provide data with more wide coverage area. Airlines policy toward not sharing FDR data adds to the challenge of real data accessibility.

7. Computational experiments

Few ATM applications use basic kinematic TPs that directly model the path characteristics of the aircraft, without attempting to model the underlying physics. Flight management systems and

accurate ground-based TPs, however, use the well-known aircraft point-mass model: a three degree of freedom model that assumes aircraft stability (i.e., rotational dynamics are not modelled) and therefore, only the aerodynamic, propulsive, and external forces (e.g., due to the gravity) are taken into account. This kinetic approach is considered accurate enough for on-board trajectory planning and all ground-based ATM applications (or hybrid applications) [4, 22]. In this point-mass model, the centre of mass is considered as the rotational centre where all forces apply. A further simplification of the three degrees of freedom point-mass model in a vertical plane results in the so-called gamma-command model [5]. The vertical equilibrium is assumed in the gamma-command model. This is the model considered in this PhD.

8. Results

This section indicates the results obtained for the simulated and real measurements. The focus is on the real-time guidance mode identification, real-time flap deployment moment estimation, the impact of parametric model mismatch, and robust filtering approach.

8.1 Validation trajectories

Validation trajectories are provided in two categories: i) 3D trajectories generated by the emulator; ii) 4D trajectories gathered from secondary radar (e.g., ADS-B data from FlightRadar24).

In the simulator, a trajectory is unequivocally specified by a sequence of phases, described by two guidance commands and an end condition. Such definition provides the three key ingredients to simulate a realistic trajectory:

1. Trajectory phases: The vertical profile of the trajectory is split in a finite number of phases. Each phase is specified by two guidance commands and an end condition. Different phases can also be used to model different flaps and/or landing gear configurations or engine thrust ratings.
2. Guidance commands and parameters: Guidance commands steer the aircraft through elevator and throttle. At each phase the parameters are used to compute the control vector,$u = [\gamma, \pi]^T$ (refer to Table I).
3. End condition: To model the transition between phases, where guidance commands and/or aerodynamic conditions (flaps/slats, landing gear position, etc) change. As an example, consider a phase where the two commands are constant Mach and idle thrust (MACH-THR), until the moment that calibrated airspeed achieves a given value (i.e., reaching that specific CAS is the phase end condition); then, the aircraft is flown at constant calibrated airspeed and constant vertical speed, being the new phase commands (VS-CAS).

8.2 Real-time guidance mode identification

8.2.1 Emulated trajectories

A set of six representative validation trajectories (VTs) are considered: four descents and two climbs. A brief description of these VTs is given in Tables 2-7. The initial conditions (IC) of the numerical integration are taken above the runway, leading to a forward integration for climbs and a backwards integration for descents. Thus, the sequence of phases in these tables is always given from the runway to cruise. Notice the IC for VT5 and VT6, where $h_p = 50$ft including, thus, the final descent/initial climb. FL stands for flight level. In the vertical profiles, ΔS refers to the distance to go (along path distance) of an aircraft during a given phase.

In the first four VTs, “CLEAN-UP” refers to the case where flaps/slats and landing gear are not deployed. For the last two VTs, which include lower altitudes down to the runaway, the flaps/slats (i.e., the most relevant positions in Airbus are modelled as “FULL”, “CONF 3, 2, 1”, or “CLEAN” to guide

the aircraft) and landing gear (i.e., “DOWN” or “UP”) are progressively retracted in the take-off and initial climb, and progressively deployed in the final approach and landing phase.
In fact, flaps/slats deployment is needed to increase the airfoil camber and the wet surface of the wing. It consequently leads to an aerodynamic drag force increase. While in aircraft descents all flap/slat positions are used, a limited number of positions are enough to guide the aircraft during the take-off. For most Airbus models there are 5 different configurations “CONF 1, “CONF 1+F”, “CONF 2”, “CONF 3”, and “FULL”. Take-offs are typically performed at “CONF1+F” or “CONF2” and higher configurations are only used in very specific or exceptional situations, due to the high induced drag, which significantly degrades the climb performance. Landings are typically performed in “CONF 3” or “FULL”.
Fig. 3 illustrates the simulated flight data, including altitude, true airspeed, calibrated airspeed, and Mach number versus distance to go. The vertical purple lines indicate the end of each phase. Because a backwards integration is used for descent profiles, the distance to go values are negative.
To further complement the information provided in Tables 2-7 and Figure 3, more details are given in the sequel:

VT1: This VT illustrates a typical early descent trajectory, where the aircraft starts to descend before reaching the planned top of descent. In this situation, the FMS typically commands a descent at constant vertical speed to intercept the planned path from below. In our VT, this segment is modelled at constant calibrated airspeed, and it is followed by a sequence of phases where the aircraft flies at idle thrust and decelerates to reach 3000ft at 230kt in clean configuration and landing gear up.

VT2 and VT3: These trajectories illustrate two typical descents down to 3000 ft. Both trajectories follow a typical MACH-THR, CAS-THR descent at idle thrust down to FL100. Besides the Mach-CAS values chosen for this initial descent, the main difference between both VTs is on the final part of the trajectory, from FL100 down to 3000ft. While in VT2 the elevator command is on the FPA and the throttle is settled to keep the constant calibrated airspeed, VT3 divides this last part into two phases, where the throttle is fixed to idle and the elevator either controls the calibrated airspeed, or reduces the speed, respectively. Both VTs are flown in clean configuration and landing gear up.

VT4: The fourth VT illustrates a typical CAS-THR, MACH-THR climb trajectory starting at 250 kt and 2300 ft above the runway, until the cruise altitude is reached, considering a clean flaps/slats configuration and landing gear up. In this climb profile, the throttle is always set at the highest rate, assuming maximum climb thrust. The other actuator (i.e., the elevator) is dedicated to control the aircraft acceleration/speed.

VT5 and VT6: These VTs illustrate representative descent and climb trajectories at lower altitudes (between FL100 and 50ft above the runway). For these trajectories, high-lift devices and landing gear deployment are modelled. The descent (VT5) starts with idle thrust and constant speed/deceleration (phases 8 and 7). The first flaps/slats position is deployed while the elevator controls the constant vertical speed and the speed is managed by the throttle (VS-CAS). In the subsequent phases, flaps/slats positions are progressively deployed, with the elevator commanding a constant ground FPA (assuming an instrumental landing system glide path is flown), while the throttle commands different deceleration rates until phase 1, where a constant calibrated airspeed is kept. Landing gear is deployed in phases 1-2-3. In VT6, the throttle is always set at the maximum rate and the acceleration/speed is controlled by the elevator. Flaps/slats positions are progressively retracted during this climb and gear is always up.

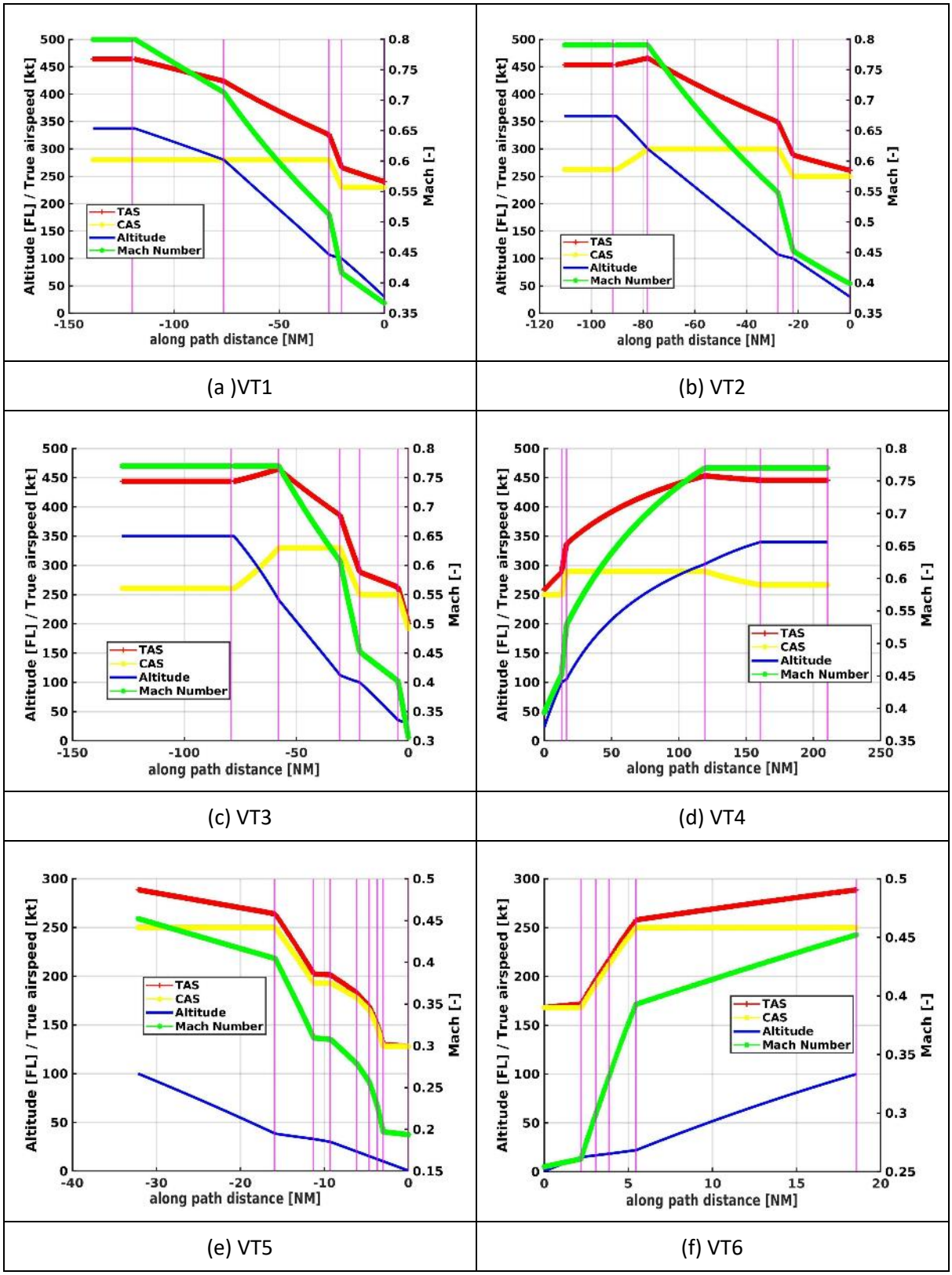

(a)VT1 (b) VT2

(c) VT3 (d) VT4

(e) VT5 (f) VT6

Fig. 3: Validation trajectories.

Table 2: Vertical descent profile specification of VT1.

IC: $h_p = 3000\,\text{ft}$, $s = 0\,\text{NM}$, $v_{\text{CAS}} = 230\,\text{kt}$, $m = 60000\,\text{kg}$

Phase	GM	Command1	Command2	End Condition	Configuration
1	CAS-THR	$\bar{v}_{\text{CAS}} = 230\,\text{kt}$	$\bar{\pi} = 0$	$h_p = \text{FL100}$	CLEAN-UP
2	DEC-THR	$\bar{k} = 0.3$	$\bar{\pi} = 0$	$v_{\text{CAS}} = 280\,\text{kt}$	CLEAN-UP
3	CAS-THR	$\bar{v}_{\text{CAS}} = 280\,\text{kt}$	$\bar{\pi} = 0$	$h_p = \text{FL280}$	CLEAN-UP
4	VS-CAS	$\bar{v}_h = -1000\,\text{ft/min}$	$\bar{v}_{\text{CAS}} = 280\,\text{kt}$	$M = 0.8$	CLEAN-UP
5	ALT-MACH	$\bar{v}_h = 0$ $(h_p = \text{FL360})$	$\bar{M} = 0.8$	$\Delta s = 20\,\text{NM}$	CLEAN-UP

Table 3: Vertical descent profile specification of VT2.

IC: $h_p = 3000\,\text{ft}$, $s = 0\,\text{NM}$, $v_{\text{CAS}} = 250\,\text{kt}$, $m = 58000\,\text{kg}$

Phase	GM	Command1	Command2	End Condition	Configuration
1	FPA-CAS	$\bar{\gamma}_g = -3\,\text{deg}$	$\bar{v}_{\text{CAS}} = 250\,\text{kt}$	$h_p = \text{FL100}$	CLEAN-UP
2	DEC-THR	$\bar{k} = 0.3$	$\bar{\pi} = 0$	$v_{\text{CAS}} = 300\,\text{kt}$	CLEAN-UP
3	CAS-THR	$\bar{v}_{\text{CAS}} = 300\,\text{kt}$	$\bar{\pi} = 0$	$h_p = \text{FL300}$	CLEAN-UP
4	MACH-THR	$\bar{M} = 0.8$	$\bar{\pi} = 0$	$h_p = \text{FL360}$	CLEAN-UP
5	ALT-MACH	$\bar{v}_h = 0$ $(h_p = \text{FL360})$	$\bar{M} = 0.8$	$\Delta s = 20\,\text{NM}$	CLEAN-UP

Table 4: Vertical descent profile specification of VT3.

IC: $h_p = 3000\,\text{ft}$, $s = 0\,\text{NM}$, $v_{\text{CAS}} = 192\,\text{kt}$, $m = 53000\,\text{kg}$

Phase	GM	Command1	Command2	End Condition	Configuration
1	DEC-THR	$\bar{k} = 0.3$	$\bar{\pi} = 0$	$v_{\text{CAS}} = 250\,\text{kt}$	CLEAN-UP
2	CAS-THR	$\bar{v}_{\text{CAS}} = 250\,\text{kt}$	$\bar{\pi} = 0$	$h_p = \text{FL100}$	CLEAN-UP
3	DEC-THR	$\bar{k} = 0.3$	$\bar{\pi} = 0$	$v_{\text{CAS}} = 330\,\text{kt}$	CLEAN-UP
4	CAS-THR	$\bar{v}_{\text{CAS}} = 330\,\text{kt}$	$\bar{\pi} = 0$	$M = 0.77$	CLEAN-UP
5	MACH-THR	$\bar{M} = 0.77$	$\bar{\pi} = 0$	$h_p = \text{FL350}$	CLEAN-UP
6	ALT-MACH	$\bar{v}_h = 0$ $(h_p = \text{FL350})$	$\bar{M} = 0.77$	$\Delta s = 50\,\text{NM}$	CLEAN-UP

Table 5: Vertical climb profile specification of VT4.

IC: $h_p = 2300\,\text{ft}$, $s = 0\,\text{NM}$, $v_{\text{CAS}} = 250\,\text{kt}$, $m = 77000\,\text{kg}$

Phase	GM	Command1	Command2	End Condition	Configuration
1	CAS-THR	$\bar{v}_{\text{CAS}} = 250\,\text{kt}$	$\bar{\pi} = 1$	$h_p = \text{FL100}$	CLEAN-UP
2	ACC-THR	$\bar{k} = 0.3$	$\bar{\pi} = 1$	$v_{\text{CAS}} = 290\,\text{kt}$	CLEAN-UP
3	CAS-THR	$\bar{v}_{\text{CAS}} = 290\,\text{kt}$	$\bar{\pi} = 1$	$M = 0.77$	CLEAN-UP
4	MACH-THR	$\bar{M} = 0.77$	$\bar{\pi} = 1$	$h_p = \text{FL340}$	CLEAN-UP
5	ALT-MACH	$\bar{v}_h = 0$ $(h_p = \text{FL340})$	$\bar{M} = 0.77$	$\Delta s = 50\,\text{NM}$	CLEAN-UP

Table 6: Vertical descent profile specification of VT5.

IC: $h_p = 50\,\text{ft},\ s = 0\,\text{NM},\ v_{\text{CAS}} = 128\,\text{kt},\ m = 53000\,\text{kg}$					
Phase	GM	Command1	Command2	End Condition	Configuration
1	FPA-CAS	$\bar{\gamma}_g = -3\,\text{deg}$	$\bar{v}_{\text{CAS}} = 128\,\text{kt}$	$h_p = 1000\,\text{ft}$	FULL-DOWN
2	FPA-DEC	$\bar{\gamma}_g = -3\,\text{deg}$	$\bar{k} = 0.472$	$v_{\text{CAS}} = 146.5\,\text{kt}$	FULL-DOWN
3	FPA-DEC	$\bar{\gamma}_g = -3\,\text{deg}$	$\bar{k} = 0.53$	$v_{\text{CAS}} = 165\,\text{kt}$	CONF3-DOWN
4	FPA-DEC	$\bar{\gamma}_g = -3\,\text{deg}$	$\bar{k} = 0.683$	$h_p = 2000\,\text{ft}$	CONF2-UP
5	FPA-DEC	$\bar{\gamma}_g = -3\,\text{deg}$	$\bar{k} = 0.76$	$h_p = 3000\,\text{ft}$	CONF1-UP
6	VS-CAS	$\bar{v}_h = -1000\,\text{ft/min}$	$\bar{v}_{\text{CAS}} = 193\,\text{kt}$	$\Delta s = 50\,\text{NM}$	CONF1-UP
7	DEC-THR	$\bar{k} = 0.3$	$\bar{\pi} = 0$	$v_{\text{CAS}} = 250\,\text{kt}$	CLEAN-UP
8	CAS-THR	$\bar{v}_{\text{CAS}} = 250\,\text{kt}$	$\bar{\pi} = 0$	$h_p = \text{FL100}$	CLEAN-UP

Table 7: Vertical climb profile specification of VT6.

IC: $h_p = 50\,\text{ft},\ s = 0\,\text{NM},\ v_{\text{CAS}} = 158\,\text{kt},\ m = 77000\,\text{kg}$					
Phase	GM	Command1	Command2	End Condition	Configuration
1	CAS-THR	$\bar{v}_{\text{CAS}} = 158\,\text{kt}$	$\bar{\pi} = 1$	$h_p = 1500\,\text{ft}$	CONF2-UP
2	ACC-THR	$\bar{k} = 0.3$	$\bar{\pi} = 1$	$v_{\text{CAS}} = 172\,\text{kt}$	CONF2-UP
3	ACC-THR	$\bar{k} = 0.3$	$\bar{\pi} = 1$	$v_{\text{CAS}} = 212\,\text{kt}$	CONF1-UP
4	ACC-THR	$\bar{k} = 0.3$	$\bar{\pi} = 1$	$v_{\text{CAS}} = 250\,\text{kt}$	CLEAN-UP
5	CAS-THR	$\bar{v}_{\text{CAS}} = 250\,\text{kt}$	$\bar{\pi} = 1$	$h_p = \text{FL100}$	CLEAN-UP

8.2.2 Further Assumptions

According to Table I, $N = 25$ guidance pairs are considered. Among these modes, 13 are related to modes with retracted configurations, and 12 consider different positions of flap/slats and landing gear---named as “non-clean”---to emulate realistic flight phases. Among all pairs, ALT-SPD is the only one with always “clean” configuration. The drag coefficient (considered known) must be computed to obtain the aerodynamic drag force. From [19], such a drag coefficient is defined considering “clean” or “non-clean” configurations. The goal is to assess the EKF-IMM capabilities to distinguish between both configurations. It is worth mentioning that the throttle is either set to 1 for climbs (maximum rate) or 0 for descents (minimum rate) when THR is an active mode. p is also assumed to be known.

The case studies presented in this section assume no winds and ISA conditions. Then, for altitudes below the tropopause altitude, $\tau_h = -\lambda_\tau$ in eq.6 ($\lambda_\tau$is the temperature lapse rate). In hydrostatic equilibrium and regardless of the pressure altitude, $p_h = -\rho g$, where the density of the air is $\rho = \frac{p}{R\tau}$.

Noting that $\dot{h}$ and v_h depend on temperature and its deviation $\Delta\tau$, the latter in ISA conditions is 0 K, then $h_p = h$ and $v_h = \dot{h}$.

Within the EKF-IMM, a time-invariant transition probability matrix is considered, with $r_{ji} = 0.02$ for $j \neq i$ and $r_{ii} = 0.98$. The initial system state x_0 can be obtained from measurements except for the aircraft mass. The initial aircraft mass is considered to be shared by the airline (airlines can deliver it depending on their policy and data confidentiality).

Results for both GM identification and state estimation are provided hereafter. To obtain statistically meaningful results, 500 Monte Carlo (MC) runs are performed. The average root mean square error (RMSE) over the trajectory is taken as the measure of state estimation performance. For GM identification, the measure of performance is the percentage of the trajectory time where the

algorithm provides an erroneous identification, denoted e_{ident}. The IMM-based GM identification results are summarised in Table 8.

Table 8: Average RMSE and guidance mode identification IMM-based results for the six representative VTs.

	VT1	VT2	VT3	VT4	VT5	VT6
e_{ident}	2.81 %	3.00 %	0.08 %	0.05 %	7.26 %	0.35 %
mean-RMSE						
h	10.47 ft	11.16 ft	13.00 ft	2.78 ft	6.91 ft	1.96 ft
s	0.06 NM	0.07 NM	0.07 NM	0.02 NM	0.01 NM	0.001 NM
v	0.56 kt	0.58 kt	0.51 kt	0.49 kt	0.53 kt	0.08 kt
m	70.41 kg	51.19 kg	7.68 kg	0.87 kg	5.51 kg	0.26 kg
τ	0.24 K	0.24 K	0.28 K	0.21 K	0.39 K	0.14 K
p	33.42 Pa	42.03 Pa	49.28 Pa	23.33 Pa	34.25 Pa	13.84 Pa

First, we can clearly see the good behaviour of the proposed solution (on average) for the trajectories which do not take into account some flap/slats (and landing gear) configurations, where e_{ident} is below 0.1% for the descent VT3 and climb VT4, and below 3% for descents VT1 and VT2. For VT6, which represents an initial climb, the IMM is also performing very well, with $e_{ident} = 0.35\%$. The most challenging VT is VT5, which contains different positions of flap/slats and landing gear and illustrates a realistic final descent, for which $e_{ident} = 7.26\%$. Even if this value is significantly larger than the ones obtained for the other VTs, notice that most of the time the method correctly identifies the active GM. The latter will be further discussed when considering the estimated guidance mode versus along path distance.

A graphical representation of the GM identification performance is shown in Fig. 4, with the results given w.r.t. along path distance. This allows to clearly distinguish the different phases of the VTs and how the different GM change (depicting as well clean or non-clean configuration settings). For each VT, the upper subplot shows the true GM; the middle subplot gives the estimated GM, that is, the one with maximum probability at each time step; and the lower subplot shows the different mode probabilities as given by the filter.

First, notice the good results obtained for VT3 (Fig. 4(c)) and VT4 (Fig. 4(c)), a typical descent and climb, respectively, for which the EKF-IMM is able to correctly identify the active mode with almost no identification delay. The same for the low altitude climb in VT6 (Fig. 4(f)), where the EKF-IMM is again able to correctly identify all the GM with a very low identification delay.

Regarding the early descent VT1 (Fig. 4(a)), the EKF-IMM perfectly identifies all the phases except the fourth phase, where the aircraft is flying in VS-CAS with high-lift devices retracted. Notice that in this phase the estimated GM mainly jumps between VS-CAS-clean and VS-CAS-non-clean, which have almost the same probability, that is, those two modes are not distinct enough for the IMM. Even if such ambiguity increases the identification error, the true GM is correctly identified if we disregard the high-lift devices configuration. These jumps also influence the state estimation accuracy. Notice that this is not a problem in practice because this phase comes just after the cruise phase, therefore it is extremely unlikely that the aircraft deploys flaps/slats at such altitude and speed, indeed leading to a correct result.

The results for VT2 (Fig. 4(b)) are similar to those for VT1, that is, all phases are perfectly identified except for one, in this case the first one. Again, the guidance mode probability mainly jumps between FPA-CAS-clean and FPA-CAS-non-clean, which are not distinct enough for the IMM to correctly estimate the mode.

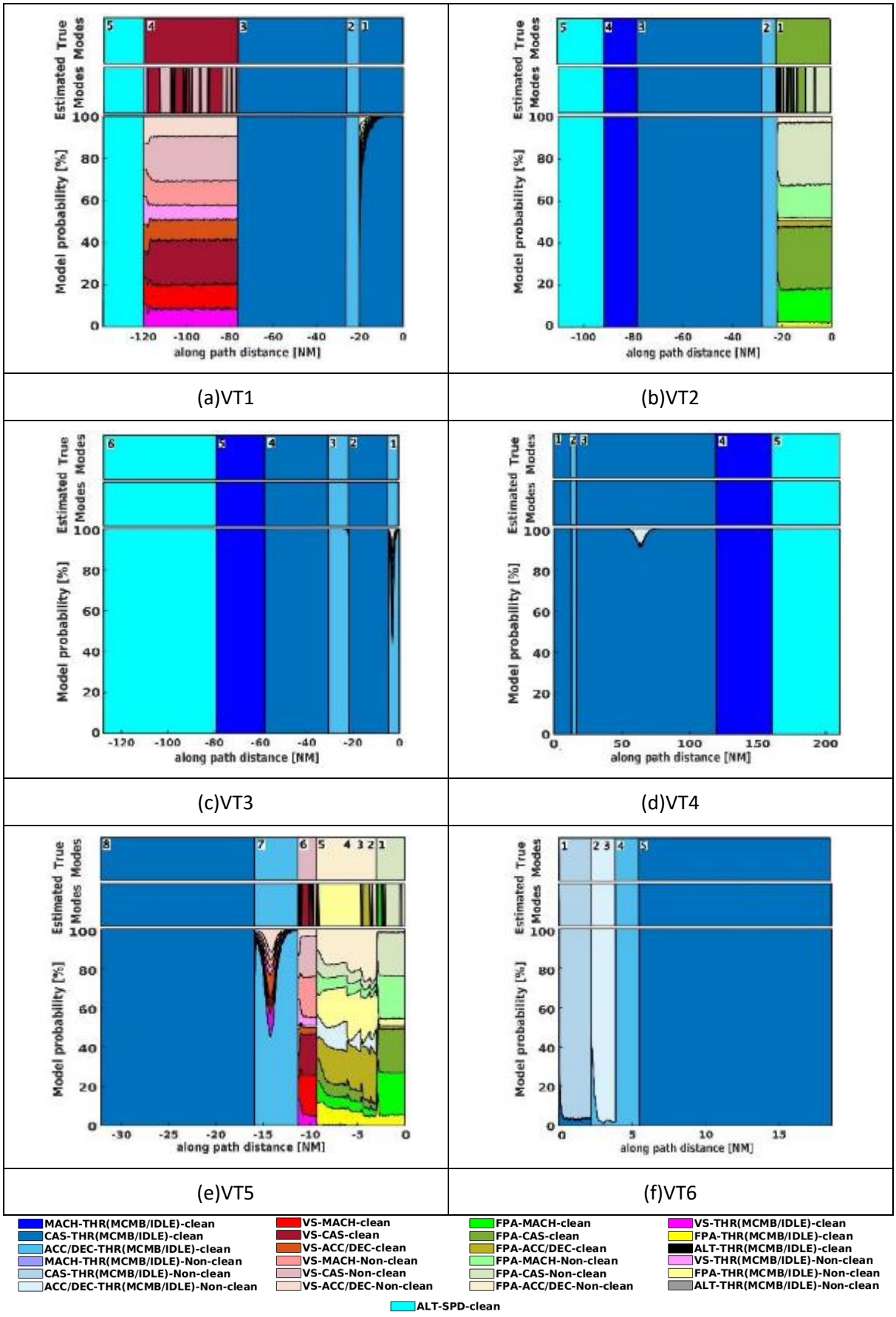

Fig. 4: For each simulated VT: (upper subplot) true GM, (middle subplot) estimated GM, and (lower subplot) IMM-based mode probabilities. GM colour code at the bottom of the figure.

The most challenging trajectory is VT5, shown in (Fig. 4(e)). This VT was selected to show the limitations of the EKF-IMM approach proposed in this article. First, notice that the algorithm is able to correctly identify the last two phases (phase 8 and 7) with clean configurations (i.e., CAS-THR and DEC-THR). But for the subsequent phases, where the aircraft is flying at VS-CAS, FPA-DEC and FPA-CAS, with different configuration settings, several identification ambiguities appear. In the sixth phase (VS-CAS) the IMM assigns almost equal probability to four modes: VS-MACH-clean, VS-CAS-clean, VS-MACH-non-clean and VS-CAS-non-clean. At the end, these modes are very similar, and being able to identify the first command is already valuable. The same happens for the following phases, for instance in the first one, where the IMM assigns almost equal probability to four modes: FPA-MACH-clean, FPA-CAS-clean, FPA-MACH-non-clean and FPA-CAS-non-clean. Although these four modes at lower altitude are very similar in terms of kinetic and potential energy rates, notice that the constant FPA outcome is correct. In conclusion, even in such challenging scenario, the IMM-based solution behaves well, but for some of the modes the configuration setting is not identifiable.

8.2.3 Real dataset

A set of FDR data of a narrow-body jet aircraft from a European airline is taken to further validate the proposed method. For this study, some challenges had to be addressed: i) the data set did not contain the (true) GM, which is the object of estimation by our application; ii) the measurements (i.e., ADS-B and EHS data) associated with the available FDR were not obtainable either; iii) a known parameters vector is required for each mode to compute the control vector; and iv) the atmospheric and weather conditions (non-ISA model) of the flights recorded in the FDR had to be taken into account. Fig. 5 shows the setup to address these challenges:

1. To address the first challenge, some close data inspection/processing was needed to **guess** the true GM executed by the aircraft from the available FDR.
2. Regarding ADS-B and EHS data: while ADS-B is automatically transmitted by the aircraft at a given frequency rate, EHS information is replied to the ATC system who initiated the interrogation [15]. Thus, the ADS-B and EHS data are broadcast by the airplane itself, and the same information is stored in the FDR, then being able to build the measurement vector.
3. The FDR data available was also analysed to obtain the corresponding parameters p, to compute the control vector.
4. For the Gaussian noise covariances, we assumed a small deviation of the initial state from its mean value, and we took into account a small initial uncertainty.
5. To address the last challenge, historical re-analysis weather data from the European Centre for Medium-Range Weather Forecasts (ECMWF) was used to provide the weather and atmospheric conditions for the particular FDR flight under analysis. The true state vector (i.e., ground truth) is generated by extracting pressure altitude, along path distance and aircraft mass directly from the FDR dataset. Notice that it contains ground speed, while true airspeed---a state variable---is computed through the effect of the wind---available from ECMWF---on the ground speed. Moreover, atmospheric conditions---temperature and pressure variables---of the true state vector are acquired from ECMWF.

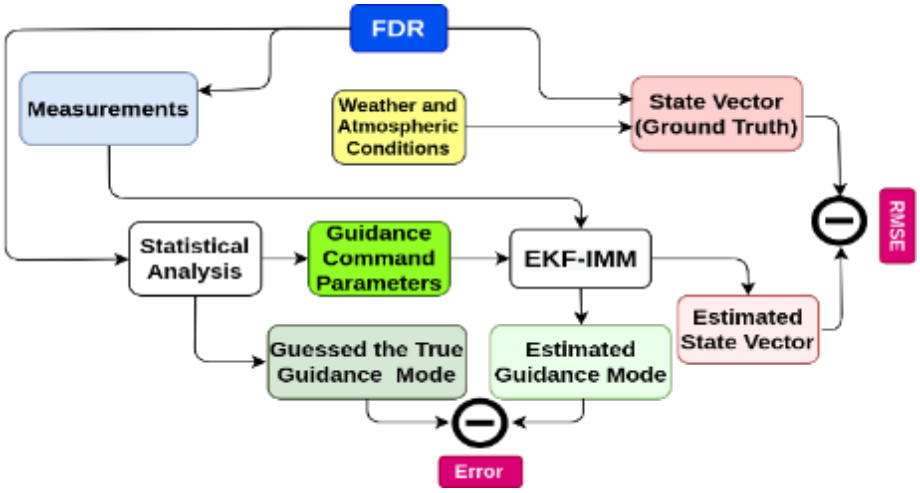

Fig. 5: Setup for the real-time processing of real data.

Two flights were considered, representative of a climb and a descent trajectory. Tables 9-10 describe the real validation trajectories 1 and 2 (RVT1 and RVT2). Notice that while guidance command parameters were known in the validation done with emulated trajectories, using real data the parameters are obtained from the measurements.

The climb trajectory (RVT1) starts at h_p =FL200 until reaching $M = 0.76$ in a constant calibrated airspeed $v_{CAS} = 280$ kt and maximum throttle rate mode (CAS-THR). Afterwards, the aircraft flies at a constant Mach number and the thrust is kept at the maximum possible rate (MACH-THR) until reaching $v_{CAS} = 255$ kt. Then, the pilot changes the mode to fly at a constant vertical speed $v_h = 1050$ ft/min with maximum thrust (VS-THR) to reduce the calibrated airspeed value until $v_{CAS} = 245$ kt. Then, a constant vertical speed and a constant calibrated airspeed are kept (VS-CAS) until FL374. The last section of the climb involves flying at a constant vertical speed with maximum thrust mode (VS-THR) to reach the cruise phase at FL380. Finally, the cruise phase (ALT-SPD) lasts for a distance of 25NM (i.e., $\Delta S = 25$ NM).

Table 9: RVT1, climb trajectory profile.

Phase	GM	Command1	Command2	End Condition	Configuration
1	CAS-THR	$\bar{v}_{\mathrm{CAS}} = 280\,\mathrm{kt}$	$\bar{\pi} = 1$	$M = 0.76$	CLEAN-UP
2	MACH-THR	$\bar{M} = 0.76$	$\bar{\pi} = 1$	$v_{\mathrm{CAS}} = 255\,\mathrm{kt}$	CLEAN-UP
3	VS-THR	$\bar{v}_h = 1050\,\mathrm{ft/min}$	$\bar{\pi} = 1$	$v_{\mathrm{CAS}} = 245\,\mathrm{kt}$	CLEAN-UP
4	VS-CAS	$\bar{v}_h = 1050\,\mathrm{ft/min}$	$\bar{v}_{\mathrm{CAS}} = 245\,\mathrm{kt}$	$h_p = \mathrm{FL374}$	CLEAN-UP
5	VS-THR	$\bar{v}_h = 1050\,\mathrm{ft/min}$	$\bar{\pi} = 1$	$h_p = \mathrm{FL380}$	CLEAN-UP
6	ALT-MACH	$\bar{v}_h = 0$ ($h_p = \mathrm{FL380}$)	$\bar{M} = 0.77$	$\Delta s = 25\,\mathrm{NM}$	CLEAN-UP

The descent profile (RVT2) begins with a cruise phase at h_p =FL320, where speed is constant ($v_{CAS} = 270$ kt and $M = 0.747$). The top of descent (TOD) is located at a distance $\Delta S = 10$ NM. After the TOD, the throttle is set to the minimum rate, which leads to an idle-thrust and constant calibrated airspeed $v_{CAS} = 270$ kt(CAS-THR) descent until FL104.8. Afterwards, the calibrated airspeed is reduced to $v_{CAS} = 250$ kt by flying a DEC-THR mode. This constant calibrated airspeed ($v_{CAS} = 250$ kt) is kept for the last two modes: in the first one, the throttle is fixed at the minimum rate (CAS-THR) to reach $h_p = 5712$ ft; in the second one, the aircraft flies with a constant FPA (FPA-CAS) to reach $h_p = 2560$ ft. In addition, high-lift devices are retracted in these two real profiles, which leads to clean configurations.

Table 10: RVT2, Descent trajectory profile.

Phase	GM	Command1	Command2	End Condition	Configuration
1	ALT-MACH	$\bar{v}_h = 0$ ($h_p = \text{FL}320$)	$\bar{M} = 0.747$	$\Delta s = 10\,\text{NM}$	CLEAN-UP
2	CAS-THR	$\bar{v}_{\text{CAS}} = 270\,\text{kt}$	$\bar{\pi} = 0$	$h_p = \text{FL}104.8$	CLEAN-UP
3	DEC-THR	$\bar{k} = 0.3$	$\bar{\pi} = 0$	$v_{\text{CAS}} = 250\,\text{kt}$	CLEAN-UP
4	CAS-THR	$\bar{v}_{\text{CAS}} = 250\,\text{kt}$	$\bar{\pi} = 0$	$h_p = 5712\,\text{ft}$	CLEAN-UP
5	FPA-CAS	$\bar{\gamma}_g = -2.15\,\text{deg}$	$\bar{v}_{\text{CAS}} = 250\,\text{kt}$	$h_p = 2560\,\text{ft}$	CLEAN-UP

Fig. 6 shows these trajectory profiles. Notice that compared to the synthetic trajectories (VT1-6), these real trajectories present much noisier profiles (i.e., clean dynamics are not available, and noisy measurements are used), which has an impact on the filter performance.

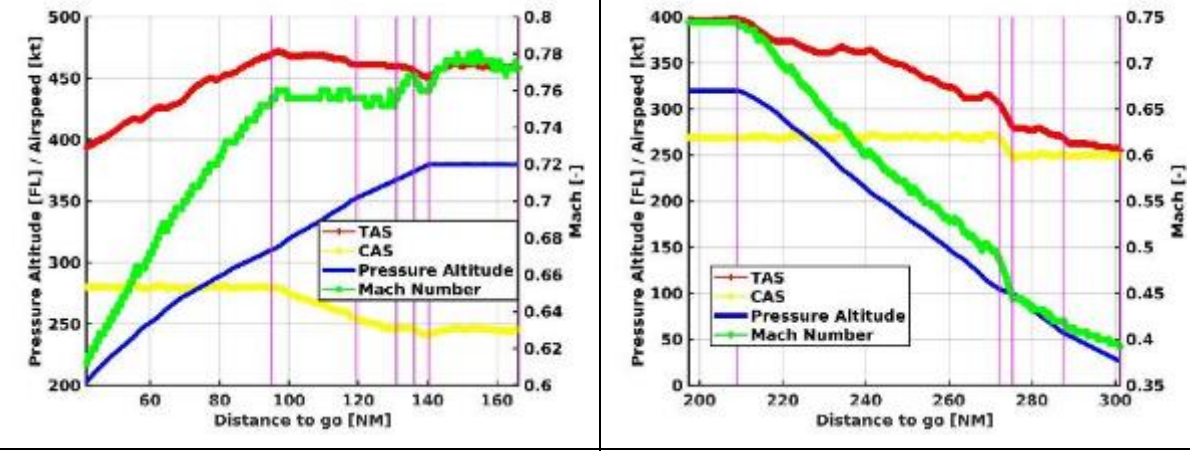

(a) RVT1 (b) RVT2

Fig. 6: Real trajectories from FDR data.

The results are shown in Fig. 7. Regarding RVT1, we firstly notice that the initial climb mode (CAS-THR) is affected by the noisy Mach number (which was not the case for the synthetic VTs). Indeed, the probability of constant Mach number is higher than flying at a constant calibrated airspeed in some short portions of this guidance mode, consequently, the EKF-IMM identifies MACH-THR. Therefore, one of the two commands is not always correctly identified. The second mode is clearly identified with a short delay. This is because a moving average filter was applied to the calibrated airspeed and Mach number in order to reduce the effects of dealing with noisy FDR data. In the third and fifth modes (VS-THR), the noisy Mach number induces again a miss-identification leading to an estimated MACH-THR mode in some short portions. This implies that only one of the two commands is not correct all the time. In some portions of the fourth mode (VS-CAS), the configuration setting is not correctly identified. Still, in such high altitudes and for the type of operations considered in this article, high-lift devices are always retracted. Therefore, the fact that the EKF-IMM cannot correctly identify the mode can be considered negligible.

In the cruise phase, altitude, speed and FPA are constant, which leads to identify several guidance modes with a close probability. Considering the summation of these probabilities leads to the correct ALT-SPD mode identification. Notice that the overall performance is reasonably good, but extracting the data from the FDR to build the scenario reduces the accuracy of the estimated active guidance modes.

The results for RVT2 show the same impact of the noisy FDR data. Again, the different guidance modes are correctly identified almost all the time, with some short miss-identifications induced by such noisy FDR data.

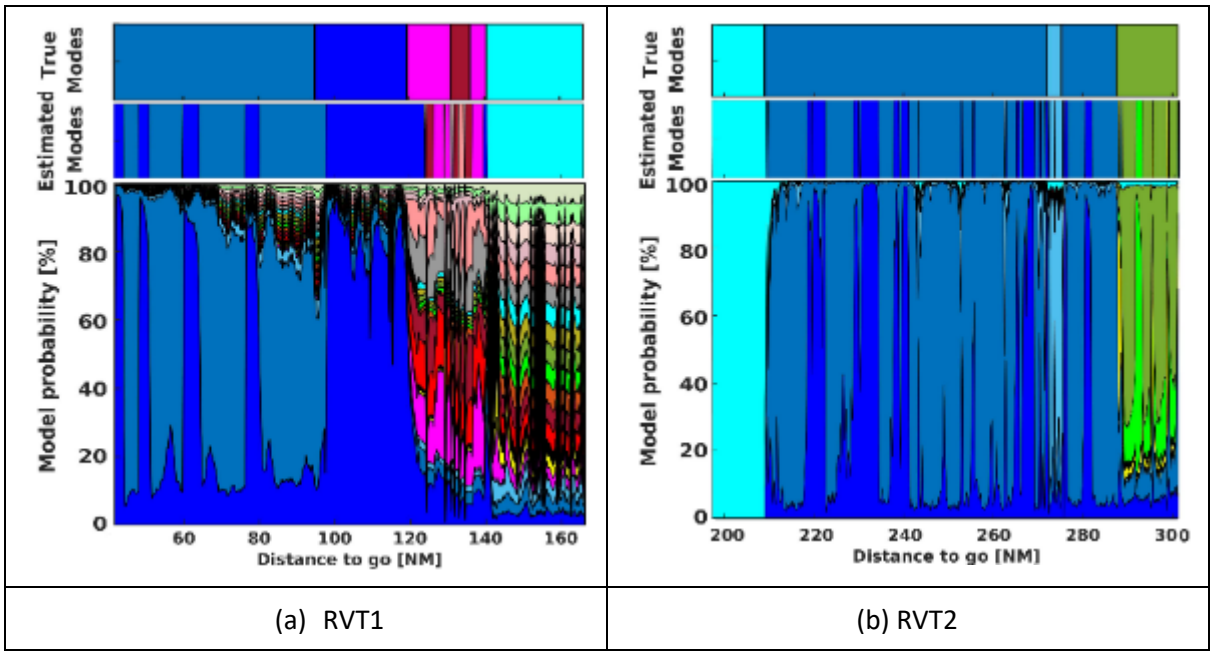

(a) RVT1 (b) RVT2

Fig. 7: For both real VTs: the guessed true GM (upper subplot), estimated GM (middle subplot), and IMM-based mode probabilities (lower subplot).

Finally, Table 11 shows the mean RMSE for each state variable, showing again a good performance of the EKF-IMM filter.

Table 11: Error in the real climb and descent profiles.

	RMSE_h	RMSE_s	RMSE_v	RMSE_m	RMSE_τ	RMSE_p
Climb	0.026 ft	3.58 NM	1.04 kt	536.2 kg	1.14 K	136.56 Pa
Descent	8.01 ft	1.97 NM	11.28 kt	55.82 kg	0.31 K	226.29 Pa

8.3 Real-time identification of flap deployment in aircraft descent

In this part of the work, the EKF-IMM method is tested assuming a hypothetical ground-based ATC decision support tool for the approach phase of the flight. It focuses on the moment that high-lift devices are deployed on descending aircraft trajectories. In fact, the EKF-IMM filter is used to identify, in real-time, the high-lift devices deployment moment

The synthetic Measurements feed the proposed filtering technique. We focus exclusively to detect the moment the first high-lift configuration is deployed (i.e., the transition from what is typically called “clean” configuration, to the first high-lift configuration setting). Then, the goal is to resort to real-time filtering techniques in order to recursively estimate the aircraft states and high-lift devices deployment moment. A fundamentally different approach is proposed, where there is no need of training data, as it relies on model-based techniques. The outcome of this study could help to develop future ground-based monitoring tools, aiming at detecting atypical trajectories and/or preventing

unstabilised approaches. It could as well enhance ground-based trajectory prediction algorithms that are enablers of a wide range of ATM applications: from air traffic control decision support tools (such as arrival managers); to ground-based safety nets or separation monitoring tools (such as Medium-Term Conflict Detection systems).

8.3.1 High-lift Devices

Aeroplanes are typically equipped with high-lift devices, which are designed to increase the maximum lift coefficient of the wing. This increase in maximum lift reduces the stall speed and therefore, allows the aircraft crew to fly the aircraft at lower speeds and, ultimately, reduce the take-off and landing distances. These devices also increase (significantly) the aerodynamic drag and consequently, are only and specifically used in the take-off and initial climb; and final stages of the approach and landing.

There are many types of such devices and the ones typically equipping modern airliners are the flaps (mounted in the trailing edge of the wing) and the slats (in the leading edge). Essentially, these devices increase the camber of the airfoil; and/or increase the wet surface of the wing (typically increasing the chord); and/or perform some control or effect on the boundary layer behaviour [23].

High-lift devices typically have different positions or configurations and are progressively deployed during the approach. Similarly, an aeroplane takes-off with a given high-lift device configuration and the crew progressively retracts them during the initial climb. The configuration where all high-lift devices are retracted is typically called **clean configuration**, and other configurations will receive different operational names depending on the aircraft type.

For example, for most Airbus models there are 5 different configurations CONF 1, CONF 1+F, CONF 2, CONF 3, and FULL. Take-offs are typically performed at CONF1+F or CONF2 and higher configurations are only used in very specific or exceptional situations, due to the high induced drag, which significantly degrades the climb performance. CONF1+F deploys (partially) slats and flaps. During an approach, CONF 1 is initially selected (which deploys partially slats) and then CONF 2 follows. Landings are typically performed in CONF 3 or FULL. Boeing aircraft, in turn, use a different nomenclature: for the B777 or B787, for instance, Flap 1 (only slats extended), Flaps 5 (slats and flaps), Flaps 15, Flaps 20... Yet, the operation is similar.

Each high-lift device configuration has a minimum and maximum speed where it can be operated and the pilots typically deploy/retract high-lift devices when reaching a certain speed and/or altitude, according to the aircraft SOP. Yet, the exact moment where they are deployed/retracted may vary even for the same aircraft model and same crew flying that aircraft. In fact, as long as these devices are operated within the speed minimum/maximum range, the crew can deploy/retract high-lift devices sooner or later. Many environment variables affect the exact moment the crew will use these devices, such as weather (especially in gusting wind conditions), obstacles below the flight path, actual climb/descent performance, but also, how **busy** is the crew in performing other tasks (i.e., communicating with air traffic control, executing more or less complex depart/approach procedures, interacting with the Flight Management Systems (FMS), etc).

As commented before, aerodynamic drag is increased when high-lift devices are used. Indeed, the drag coefficient is increased because of higher induced drag caused by the distorted span-wise lift distribution on the wing with flaps extended [23]. To a lesser extent, the parasite drag coefficient might also increase. Thus, aircraft performance models typically specify different drag coefficient parameters for each high-lift device configuration of the aircraft.

8.3.2 Simulated Setup

The trajectory simulator generates flight data which contains the same information that could be obtained from ADS-B and a selective mode transponder (Mode S) receiver. The trajectories are divided into several flight phases, each one expressed in terms of a parametrised guidance mode being targeted and an end condition to be met. The initial condition of the trajectories profile can be described as the initial mass of the aircraft, the pressure altitude, the speed and the geometric position. The profile starts at the initial condition and the trajectory is numerically integrated according to the guidance mode until reaching the end condition. In turn, this end condition is used as the initial condition for the next trajectory phase [1]. Thus, the starting time of each phase is the ending time of the previous one. The simulator is based on BADA aircraft performance models [19].

Table 12: Vertical profile specification of the Validation Trajectory (VT1)

Phase	Guidance Mode	Mode1	Mode2	End Condition	Configuration	Landing Gear
1	THR-CAS	Idle	250 kt	$h_p = 4000$ ft	CLEAN	UP
2	THR-DEC	Idle	0.3	$CAS = 193$ kt	CLEAN	UP
3	VS-CAS	−500 ft/min	193 kt	$\Delta s = 2$ NM	CONF 1	UP
4	FPA-DEC	−3°	0.76	$h_p = 2000$ ft	CONF 1	UP
5	FPA-DEC	−3°	0.6835	$h_p = 1500$ ft	CONF 2	UP
6	FPA-DEC	−3°	0.53	$CAS = 147$ kt	CONF 3	DOWN
7	FPA-DEC	−3°	0.472	$CAS = 128$ kt	FULL	DOWN
8	FPA-CAS	−3°	128 kt	$h_p = 50$ ft	FULL	DOWN

Table 13: Vertical profile specifications of the Validation Trajectories (VT2,VT3,VT4,VT5)

Phase	Guidance Mode	Mode1	Mode2	End Condition	Flap position	LG
1	THR-CAS	Idle	250 kt	$h_p = 4000$ ft	CLEAN	UP
2	THR-DEC	Idle	0.3	$CAS = v2$	CLEAN	UP
3	THR-DEC	Idle	0.3	$CAS = 193$ kt	CONF 1	UP
4	VS-CAS	−500 ft/min	193 kt	$\Delta s = 2$ NM	CONF 1	UP
5	FPA-DEC	−3°	0.76	$h_p = 2000$ ft	CONF 1	UP
6	FPA-DEC	−3°	0.6835	$h_p = 1500$ ft	CONF 2	UP
7	FPA-DEC	−3°	0.53	$CAS = 147$ kt	CONF 3	DOWN
8	FPA-DEC	−3°	0.472	$CAS = 128$ kt	FULL	DOWN
9	FPA-CAS	−3°	128 kt	$h_p = 50$ ft	FULL	DOWN

Table 14: Vertical profile specification of the Validation Trajectories (VT6,VT7,VT8)

Phase	Guidance Mode	Mode1	Mode2	End Condition	Flap position	LG
1	THR-CAS	Idle	250 kt	$h_p = 4000$ ft	CLEAN	UP
2	THR-DEC	Idle	0.3	$CAS = 193$ kt	CLEAN	UP
3	VS-CAS	−500 ft/min	193 kt	$\Delta s = s3$	CLEAN	UP
4	VS-CAS	−500 ft/min	193 kt	$\Delta s = s4$	CONF 1	UP
5	FPA-DEC	−3°	0.76	$h_p = 2000$ ft	CONF 1	UP
6	FPA-DEC	−3°	0.6835	$h_p = 1500$ ft	CONF 2	UP
7	FPA-DEC	−3°	0.53	$CAS = 147$ kt	CONF 3	DOWN
8	FPA-DEC	−3°	0.472	$CAS = 128$ kt	FULL	DOWN
9	FPA-CAS	−3°	128 kt	$h_p = 50$ ft	FULL	DOWN

Table 15: End condition parametrisations

	VT2	VT3	VT4	VT5	VT6	VT7	VT8
$v2$	230 kt	210 kt	220 kt	200 kt			
s3					0.5 NM	0.75 NM	1 NM
s4					1.5 NM	1.25 NM	1 NM

Table 12 gives details on the typical descending profile for the first validation trajectory (VT1), including the corresponding guidance modes and their associated values, the end condition, the flap position, and the landing gear position. In this VT, the pilot decides to start using flaps at phase 3, and simultaneously switches from flying with idle thrust and deceleration to constant VS and constant CAS. Table 13 gives the typical profiles associated to VT 2 to 5, where the flaps are deployed without changing the guidance mode. In this case the flaps are deployed while flying in idle thrust and deceleration mode. The difference among VT 2 to 5 is the end condition of the second phase (i.e., CAS = = $v2$, with the corresponding values summarised in Table 15.
Table 14 concerns the last three typical VT profiles (VT 6 to 8), for which the flaps are deployed while flying at constant VS and constant CAS, at three different moments (refer to the end condition $\Delta s = s3$ and $\Delta s = s4$ in Table 14, and the corresponding values summarised in 15.

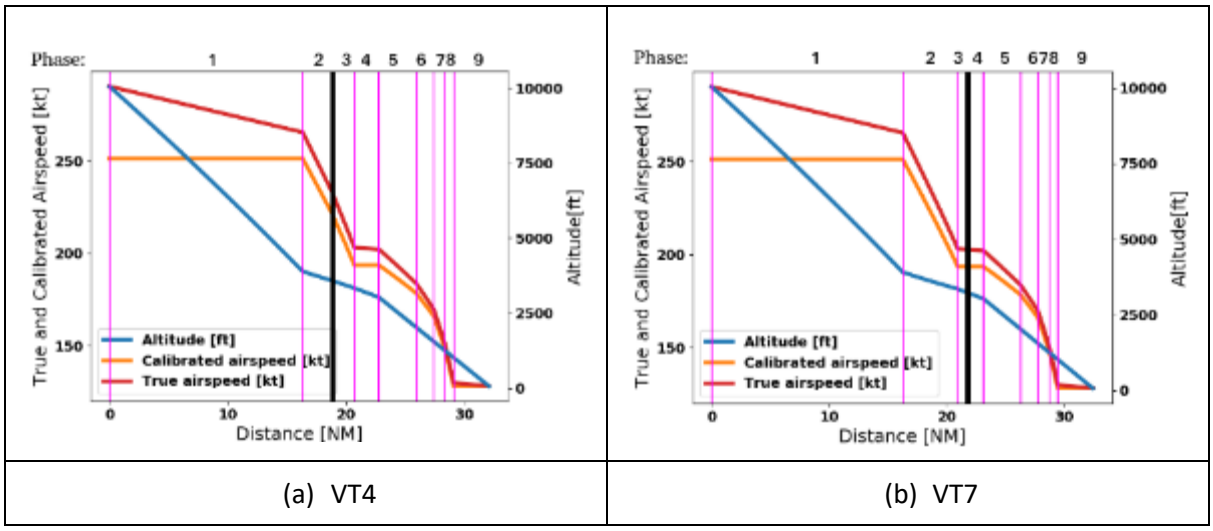

(a) VT4 (b) VT7

Fig 8: Descending profiles for VT4 and VT7. Start of the different phases indicated with the pink vertical lines, and flap deployment illustrated by the vertical black line.

Figure 8 illustrates the geometric altitude, true airspeed, and CAS for the descending profiles associated to VT4 and VT7, as an example of the 8 VT. The vertical pink lines show the start time of each phase of the profile, and the vertical black line indicates the flap deployment moment.

8.3.3 Results

In the simulations we consider the general nonlinear discrete SSMs, taking into account that the measurement noise is a zero-mean Gaussian with known covariance. Recall that one of the outputs of the EKF-IMM is the model probability, which is exploited in this contribution for flap deployment identification. For each VT we perform 1000 Monte Carlo runs in order to obtain statistically meaningful results. The average model probability around the flap deployment moment (two phases at the vicinity of the flap deployment moment), for the different VT, is shown in Figure 9. Indeed, results Figure 2 focus on the flap deployment moment, but the whole trajectory is estimated. For each VT, the upper subplot shows the real guidance mode, and the lower subplot the average estimated

mode probability. It is easy to see that in most of the cases the EKF-IMM is able to estimate the correct guidance mode (i.e., taking the model with maximum probability among the pool of possible modes). Figure 9 also shows the average estimated flap deployment moment (vertical black dashed line). Notice that in order to avoid false alarms, or equivalently, to increase the method's robustness, this value is computed using a moving average of the EKF-IMM outcome mode probabilities, with a window size equal to $N = 5$ samples. Obviously, there exists a performance versus robustness trade-off which requires a dedicated study (i.e., w.r.t. the window size, the flap deployment moment, the system parameters, etc.) and is left for future work.

The moving average method implicitly induces a method response delay, that is why in subplots (a) to (e) in Figure 9 there is a slight shift to the right w.r.t. the true flap deployment time instant. Indeed, this is not only because of the moving average but also because the EKF-IMM also needs a short time lapse to adapt to the new mode when switching between two different configuration settings. It is interesting to notice that in the last three VT, that is, VT6 to VT8, the IMM is not able to correctly decouple the identification of VS-CAS clean mode from the VS-CAS CONF1 mode. This has a direct impact on the results, and the high-lift device deployment moment estimate appears before the real mode change.

To further complete the previous results a box-and-whiskers plot is shown in Figure 10 to be able to better understand the flap deployment moment estimation error (in seconds in the plot) for all VTs. For each VT, the bottom and top of the box represent the first and third quartiles, respectively. The lines extending vertically from the boxes (whiskers) indicate the variability outside these quartiles, while the ends of the whiskers represent the 1.5 interquartile range of the first and third quartile. Finally, the red line inside the box is provides the median, and outliers are represented in red points.

It is interesting to acknowledge again a significantly different IMM behaviour depending on the descent configuration. Indeed, because of the moving average procedure using $N = 5$ samples, one would expect the average estimation error to be between 0 and -5 seconds, which is the case for VT2, VT4 and VT5, but the error slightly increases for VT1 and VT3, meaning that the IMM takes some extra time to respond to the mode change. As already stated, because the IMM is not able to correctly decouple the VS-CAS clean mode from the VS-CAS CONF1 mode, then the error is positive for VT6 to VT8. In any case, the average method performance is good enough to validate the proposed methodology.

In this paper, the metric to measure the filter performance is the difference between the real and estimated deployment time, in seconds. If we take the true airspeed of the aircraft at the moment CONF 1 is deployed, the error in distance is always below 1 NM. These are promising results, taking into account the performance of similar studies found in the literature, such as [24]. We have to keep in mind, however, that in this paper the validation has been done with a few number of simulated trajectories.

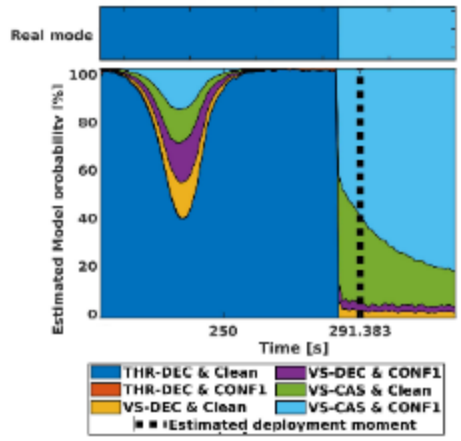

(a) VT1

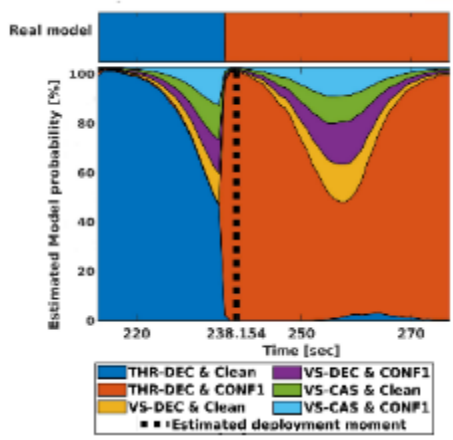

(b) VT2

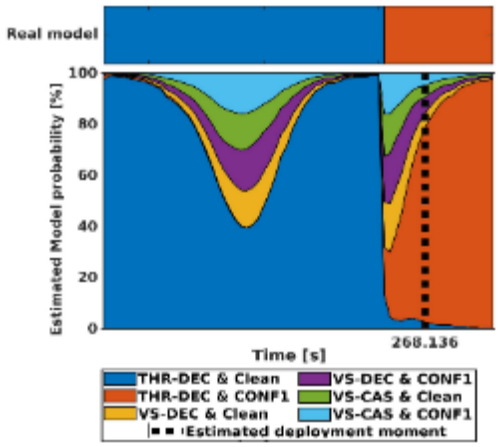

(c) VT3

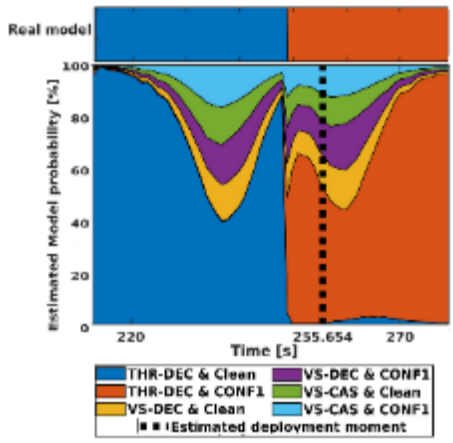

(d) VT4

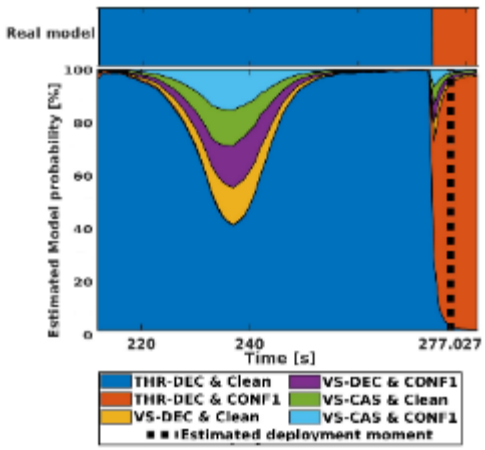

(e) VT5

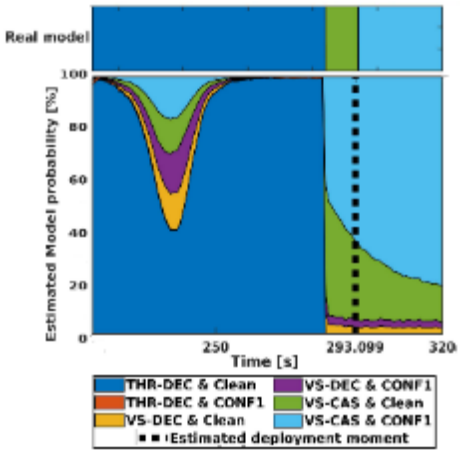

(f) VT6

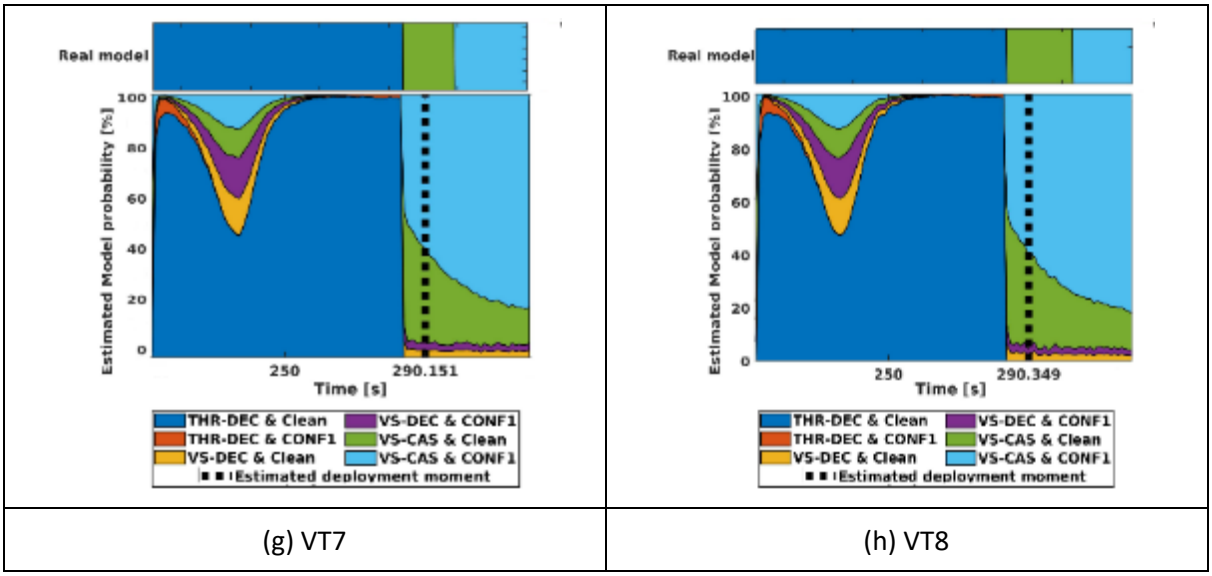

(g) VT7 (h) VT8

Fig. 9: Considering the trajectory region around the flap deployment moment, each subplot provides, for each validation trajectory (VT): 1) the real guidance mode, 2) average estimated model probability, and 3) the estimated flap deployment moment.

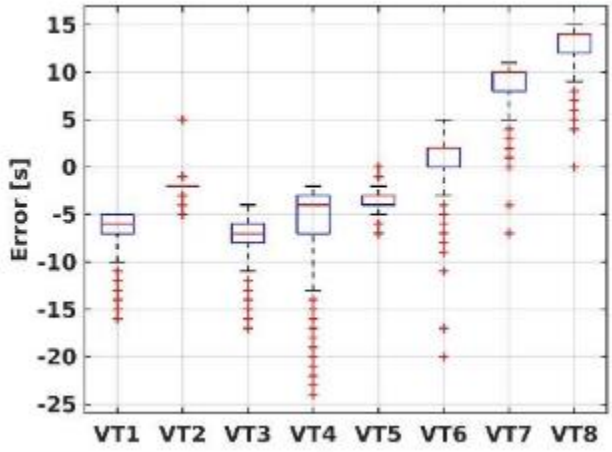

Fig. 10: Estimation error of flap deployment moment.

8.4 The impact of parametric model mismatch and constrained IMM filtering

The impact of parametric model mismatch and the robust filter are the focus of several studies [25] in this PhD. In any case, either for linear or nonlinear systems, standard filtering techniques typically assume a perfect knowledge of the system, i.e., known process and measurement functions, and the corresponding noise statistics, which may not be a realistic assumption in practice. That is the reason why there is a continued effort to develop robust filtering techniques. Closed-form expressions for the bias and covariance induced by a possible model mismatch are not available, being an important missing point for the correct filter design in real-life applications. We explore the impact in extended Kalman filter approximations of a parametric model mismatch on both system functions, and provide expressions for the estimator bias and covariance error induced by the mismatch (refer to [25] for mathematical details). It is known that a model mismatch may induce a significant filter performance degradation, therefore, one may expect that the command parameters misspecification (unknown or noisy inputs) clearly affects the IMM performance. A sensitivity analysis of such performance

degradation (i.e., considering possibly mismatched guidance commands) is fundamental for the design and derivation of new robust TP techniques. We further explore the impact of such model misspecification in multiple model solutions, and leverage the recently introduced linearly constrained Kalman filter to propose a robust linearly constrained IMM, which is able to mitigate the model mismatch impact on the final filter performance.

9. Analysis of the results

The mean RMSE results in Table 8 also support the good performance statement. Overall, such results show the validity of the IMM-based method for both aircraft state estimation and GM identification. But to further support the discussion, we get into each VT specificity.

We can still say that the IMM-based GM identification approach is a promising solution, given that even with real (and noisy) FDR data the filter is able to identify the correct modes almost all the time.

Moreover, the IMM filtering approach has been proposed for real-time identification of the high-lift device deployment moment in aircraft descents. The underlying idea was to exploit the fact that aircraft fly following different guidance modes (each one related to a specific dynamic model), reason why a multiple model filtering strategy must be accounted for, and study if such multiple model filters were able to identify the difference between clean and deployed high-lift configurations. The results show the good performance of the IMM-based high-lift deployment identification, being a promising solution for such application. This work could help to develop future ground-based monitoring tools, aiming at detecting atypical trajectories and/or preventing unstabilised approaches, but could enable as well advanced trajectory prediction capabilities benefiting many ATM applications.

10. Conclusions and look ahead

An executed trajectory can be defined as a sequence of consecutive guidance modes. In the vertical plane, and for each mode, two commands shall be given to specify the two path constraints to transform the DAE system into an ODE system to be numerically integrated. Guidance mode identification—the focus of this PhD—is required to boost the overall TP accuracy. An IMM-based filter was proposed to identify the active guidance mode among all possible command pairs. Several validation trajectories were considered to perform a statistically meaningful optimal EKF-IMM analysis in representative scenarios.

Kalman filter-based methods are optimal when the process and measurement noises are independent and Gaussian. Although the extended Kalman filter has been used in nonlinear systems, the particle filtering approach has become a better alternative in nonlinear and/or non-Gaussian scenarios. Particle filtering is a sequential Monte Carlo methodology based on Bayesian theory and importance sampling. Particles in particle filtering are samples of the unknown state and Bayes theorem is used to compute the particle weights. In fact, particle filtering uses the particles to represent an approximation of the posterior distribution. In other filtering methods, a linearization is applied at the vicinity of the estimated states while particle filtering is based on the approximation of the desired distribution given noisy measurements. Using particle filtering for the guidance mode identification is the final piece of the puzzle to accomplish this PhD.

Extending the high-lift deployment identification to other configuration settings containing different flap positions, and landing gear up/down is considered for future work (using the particle filtering method). Moreover, the impact of real-time guidance mode identification on the TP problem for multi-aircraft scenarios must be indicated in the future work.

11. References

11.1 Link to PhD thesis / repository

The following two links are provided for the public repository where the publishable dissertation will be stored.

https://www.tesisenred.net/

https://upcommons.upc.edu/

11.2 Associated outputs and publications

[1] Khaledian, H.; Prats, X.; Jordi , V. Advanced statistical signal processing for next generation trajectory prediction. Proceedings of 9th ICRAT 2020 - International Conference on Research in Air Transportation. 2020.

[2] Khaledian, H.; Vilà-Valls, J.; Chaumette, E.; Prats, X. On Parametric model mismatch in nonlinear EKF Approximations. Conference record of The Fifty-Fourth Asilomar Conference on Signals, Systems & Computers: November 1-5, 2020 Pacific Grove, California. Institute of Electrical and Electronics Engineers (IEEE). 2020. ISBN/ISSN: 978-0-7381-3126-9. https://ieeexplore.ieee.org/xpl/conhome/9443248/proceeding.

[3] Khaledian, H.; Prats, X.; Vilà-Valls, J. Real-time Identification of High-Lift Devices Deployment in Aircraft Descents (An Interacting Multiple Model Filtering Application Validated with Simulated Trajectories). 10th SESAR Innovation Days: 7th of December-10th of December, 2020, virtual event. Single European Sky ATM Research (SESAR). 2020. Pàgs.: 1-8.

[4] Saez, R.; Khaledian, H.; Prats, X.; Guitart, A.; Delahaye, D.; Feron, E. A Fast and flexible emergency trajectory generator: enhancing emergency geometric planning with aircraft dynamics. 14th USA/Europe Air Traffic Management Research and Development Seminar 2021 (virtual event): 20-24 September, 2021. 2021. Pàgs.: 1-10.

[5] Saez, R.; Khaledian, H.; Prats, X. Generation of emergency trajectories based on aircraft trajectory prediction. 2021 IEEE/AIAA 40th Digital Avionics Systems Conference: San Antonio, TX, USA: October 3-7, 2021. Institute of Electrical and Electronics Engineers (IEEE). 2021. pp.: 1 ~ 10. ISBN/ISSN: 9781665434218. https://ieeexplore.ieee.org/document/9594403.

[6] Advanced Statistical Signal Processing for Next Generation Trajectory Prediction. Engage KTN summer school 2021 (virtual). virtual. 30/08/2021.

[7] Advanced Statistical Signal Processing for Next Generation Trajectory Prediction. 3rd Data-driven trajectory prediction workshop (Engage thematic Challenge 2). 25/01/2021.

[8] Advanced Statistical Signal Processing for Next Generation Trajectory Prediction. Engage KTN summer school 2020 (virtual). virtual. 22/09/2020.

[9] Advanced Statistical Signal Processing for Next Generation Trajectory Prediction. Engage Thematic Challenge 2. Athens, Greece. 02/12/2019.

[10] Advanced Statistical Signal Processing for Next Generation Trajectory Prediction. Engage KTN Summer School 2019. Belgrade, Serbia. 10/09/2019.

11.3 References cited in this report

[1] R. Dalmau, M. Pérez-Batlle, and X. Prats, “Real-time Identification of Guidance Modes in Aircraft Descents Using Surveillace Data,” in Proc. of the IEEE/AIAA Digital Avionics Systems Conference, 2018.

[2] E. Casado, L. D’Alto, and M. Vilaplana, “Analysis of the impact of intent uncertainty on the accuracy of predicted trajectories for arrival management automation,” in 6th International Conference on Research in Air Transportation, 2014.

[3] D. G. Hull et al., Fundamentals of airplane flight mechanics. Springer, 2007, vol. 19.

[4] R. Dalmau, “Optimal Trajectory Management for Aircraft Descent Operations Subject to Time Constraints.” Ph.D. dissertation, Technical University of Catalonia (UPC), Barcelona, Spain, 2019.

[5] J. Bronsvoort, “Contributions to trajectory prediction theory and its application to arrival management for air traffic control,” Ph. D. thesis, 2014.

[6] E. Gallo, J. Lopez-Leones, M. A. Vilaplana, F. A. Navarro, and A. Nuic, “Trajectory computation infrastructure based on bada aircraft performance model,” in 2007 IEEE/AIAA 26th Digital Avionics Systems Conference. IEEE, 2007, pp. 1–C.

[7] R. Dalmau, J. Sun, and X. Prats, "Fuel inefficiency characterisation and assessment due to early execution of top of descents. A Case Study for Amsterdam-Schiphol Terminal Airspace using ADS-B data." in Proc. of 14th USA/Europe Air Traffic Management Research and Development Seminar 2021 (virtual event): 20-24 September, 2021. 2021.

[8] L. Crassidis and J. L. Junkins, “Optimal Estimation of Dynamic Systems,” CRC Press, Taylor & Francis Group, 2nd edition, 2012.

[9] P. S. R. Diniz, “Adaptive Filtering: Algorithms and Practical Implementation,” Springer, Switzerland, 4th edition, 2013.

[10] D. Simon, “Optimal State Estimation: Kalman, H Infinity, and Nonlinear Approaches,” Wiley InterScience, New York, USA, 2006.

[11] I. Arasaratnam and S. Haykin, “Cubature Kalman filters,” IEEE Trans. Automatic Control, vol. 54, no. 6, pp. 1254–1269, June 2009.

[12] P. M. Djuric et al., "Particle filtering." *IEEE signal processing magazine* vol. 20, no. 5, pp. 19-38, 2003.

[13] H. A. P. Blom and E. A. Bloem, “Exact Bayesian and Particle Filtering of Stochastic Hybrid Systems,” IEEE Transactions on Aerospace and Electronic Systems, vol. 43, no. 1, pp. 55–70, Jan. 2007.

[14] A. Ienkaran et al., "Discrete-time nonlinear filtering algorithms using Gauss–Hermite quadrature." in Proc. of the IEEE 95.5 (2007): 953-977.

[15] J. Sun, “Open Aircraft Performance Modeling: Based on an Analysis of Aircraft Surveillance Data.” Ph.D. dissertation, Delft University of Technology (TUDelft), Delft, Netherlands, 2019.

[16] M. N. Guerreiro, and M. C. Underwood, "Understanding extended projected profile (epp) trajectory error using a medium-fidelity aircraft simulation." in Proc. of Aviation Technology, Integration, and Operations Conference. 2018.

[17] J. Bronsvoort et al., "Real-time trajectory predictor calibration through extended projected profile down-link." in Proc. of Eleventh USA/Europe Air Traffic Management Research and Development Seminar. 2015.

[18] R. Šošovička, et al., "Estimation of aircraft performance parameters from ADS-C EPP data." in Proc. of Integrated Communication, Navigation and Surveillance Conference (ICNS). IEEE, 2015.

[19] Eurocontrol, “User manual for the base of aircraft data (BADA). revision 4.1,” Eurocontrol, Bretigny, France, Tech. Rep., 2014.

[20] “OpenSky Network,” https://opensky-network.org, 2019, accessed: August 15, 2021.

[21] “Flightradar24,” https://www.flightradar24.com, accessed: February 1, 2022.

[22] D. G. Hull et al., “Fundamentals of airplane flight mechanics.” Springer, vol. 19, 2007.

[23] M. Soler, “Fundamentals of Aerospace Engineering: An introductory course to aeronautical engineering. 2014.

[24] G. Jarry, D. Delahaye, and E. Feron. "Approach and landing aircraft on-board parameters estimation with lstm networks." in Proc. of International Conference on Artificial Intelligence and Data Analytics for Air Transportation (AIDA-AT). IEEE, 2020.

[25] H. Khaledian, J. Vilà-Valls, E. Chaumette, and X. Prats. “On Parametric Model Mismatch in Nonlinear EKF Approximations.” In Proc. of 54th Asilomar Conference on Signals, Systems, and Computers (pp. 1486-1490). IEEE.

[26] H. Georgiou et al., "Moving objects analytics: survey on future location and trajectory prediction methods." arXiv preprint arXiv:1807.04639 (2018).

[27] Y. Le Fablec et al., "Using Neural Networks to Predict Aircraft Trajectories." IC-AI. 1999.

[28] Z. Wang et al., "A hybrid machine learning model for short-term estimated time of arrival prediction in terminal manoeuvring area." Transportation Research Part C: Emerging Technologies vol. 95, pp. 280-294, 2018.

[29] Casado Magaña, Enrique Juan. “Trajectory prediction uncertainty modelling for Air Traffic Management”. Ph.D. dissertation, University of Glasgow, 2016.

[30] P. Weitz, "Determination and visualization of uncertainties in 4D-trajectory prediction." in Proc. of Integrated Communications, Navigation and Surveillance Conference (ICNS). IEEE, 2013.

[31] DP. Thipphavong et al. "Adaptive algorithm to improve trajectory prediction accuracy of climbing aircraft." Journal of Guidance, Control, and Dynamics, vol. 36, pp. 15-24, 2013.

[32] W. Liu, et al., "Probabilistic trajectory prediction and conflict detection for air traffic control." Journal of Guidance, Control, and Dynamics vol. 34, pp. 1779-1789, 2011.

[33] XR. Li et al., "Survey of maneuvering target tracking. Part V. Multiple-model methods." IEEE Transactions on Aerospace and Electronic Systems, vol. 41, no. 4, pp. 1255-1321, 2005.

[34] Q. Wang et al., "A VB-IMM filter for ADS-B data." in Proc. of 12th International Conference on Signal Processing (ICSP). IEEE, 2014.

[35] H. Khadilkar et al., "A multi-modal unscented Kalman filter for inference of aircraft position and taxi mode from surface surveillance data." in Proc. of 11th AIAA Aviation Technology, Integration, and Operations (ATIO) Conference, including the AIAA Balloon Systems Conference and 19th AIAA Lighter-Than. 2011.

[36] D. Jeon, et al., "Nonlinear aircraft tracking filter utilizing a point mass flight dynamics model." in Proc. of the Institution of Mechanical Engineers, Part G: Journal of Aerospace Engineering vol. 227, no. 11, pp.1795-1810, 2013.

[37] I. Hwang, et al., "Flight-mode-based aircraft conflict detection using a residual-mean interacting multiple model algorithm." in Proc. of AIAA guidance, navigation, and control conference and exhibit. 2003.

[38] JL. Yepes, et al., "New algorithms for aircraft intent inference and trajectory prediction." Journal of guidance, control, and dynamics, vol. 30, no. 2, pp. 370-382, 2007.

Annex I: Acronyms

Term	Definition
ADS-B	Automatic Dependent Surveillance-Broadcast
ADS-C EPP	ADS - Contract Extended Projected Profile
ATM	air traffic management
BADA	Base of Aircraft Data
BDS	Comm-B Data Selector
CDR	conflict detection and resolution
DAEs	differential-algebraic equations
DSTs	decision support tools
ECMWF	European Centre for Medium-Range Weather Forecasts
EHS	Enhanced Mode-S Surveillance
EKF	extended KF
FDR	flight data recorder
FMGS	flight management and guidance system
FMS	Flight management system
FPA	flight path angle
GM	Guidance mode
IC	initial conditions
IMM	Interacting multiple model
ISA	international standard atmosphere
KF	Kalman filter
MC	Monte Carlo
M-EKF	Mismatched EKF
MMO	maximum Mach in operations
MMSE	minimum mean square error
ODEs	ordinary differential equations
RMSE	root mean square error
SSMs	state-space models
SSR	secondary surveillance radar
TBO	trajectory-based operation
TP	trajectory prediction
VT	validation trajectory